Splitter Plate Design for Side Wall Testing in the Kirsten Wind Tunnel

Juanita Osorio Tovar

A thesis
submitted in partial fulfillment of the
requirements for the degree of

Master of Science in Aeronautics & Astronautics

University of Washington

2025

Reading Committee:

Owen J. H. Williams, Chair

Eli Livne

Program Authorized to Offer Degree:
College of Engineering,
William E. Boeing Department of Aeronautics and Astronautics

University of Washington

Abstract

Splitter Plate Design for Side Wall Testing in the Kirsten Wind Tunnel

Juanita Osorio Tovar

Chair of the Supervisory Committee:
Research Assistant Professor Owen J. H. Williams
Aeronautics & Astronautics

Half-model and side-wall balance capabilities are being developed for an ongoing High-Lift Common Research Model (CRM-HL) testing campaign at the University of Washington. As part of this effort, a well characterized splitter plate is required to provide a symmetry plane. This thesis outlines the design and testing of this splitter plate, as well as requirements to obtain a well-characterized, zero-pressure gradient, uniform, canonical turbulent boundary layer that is free of artifacts. The splitter spans the entire test section wall, avoiding the geometric chamfers, and consists of three main body plates, a rounded leading edge, trailing edge flap, and instrumentation for pressure and velocity diagnostics. The design meets requirements for flatness, stiffness, modularity, and repeatability. It also complies with the tunnel's safety standards, while adapting to the challenges of building a large-scale structure with tight tolerances using available fabrication tools. The plate will be validated via boundary layer measurements using a pitot-traverse system and static pressure taps to confirm flow uniformity over the plate and verify that the splitter enables a zero-pressure-gradient environment. The system is expected to significantly reduce experimental uncertainty and minimize biases due to interactions with the model's symmetry plane.

TABLE OF CONTENTS

LIST OF FIGURES

LIST OF TABLES

NOMENCLATURE

δ: Boundary layer thickness

δ^*: Displacement thickness

θ: Momentum thickness

u_τ: Friction velocity

ν: Kinematic velocity

y: Wall-Normal distance

u: Velocity

y^+: Non-Dimensional wall distance

u^+: Non-Dimensional velocity

κ: von Kármán constant

B: Empirical constant in the logarithmic law of the wall

η: Outer scaling wall distance

U_e: Velocity at the edge of the boundary layer

Π: Wake strength parameter

$W(\eta)$: Wake function

β: Clauser pressure gradient parameter

τ_w: Wall shear stress

$\frac{dP_e}{dx}$: Streamwise pressure gradient

K: Acceleration parameter

Re_x: X-axis position based Reynolds number

C_L: Lift Coefficient

α: Angle of attack

L: Lift

q: Dynamic pressure

A: Surface area

C_f: Skin friction coefficient

ρ: Density

A_t: Tensile stress area

A_s: Shank cross-sectional area

$\sigma_{tensile}$: Ultimate tensile strength

τ: Shear strength

F: Force

d_{minor}: Minor diameter

L_e: Thread engagement length

n: Number of threads per inch

ACKNOWLEDGMENTS

I am deeply grateful to all the people who supported and contributed to this work in many different ways. To Dr. Williams, for his invaluable guidance, thoughtful feedback, and for always seeing the person behind the engineer. I am also thankful for the knowledge and expertise shared by our mentors at Boeing. To my lab mates and friends in the Williams group—thank you for the moral support, the explanations, and the snacks.

Beyond the academic, I could not have undertaken this journey without the unwavering support and inspiration of my friends and family, both near and far. Thank you for giving me the confidence to pursue this path, for the laughter that keeps me going, and for the music that keeps me alive.

Chapter 1

INTRODUCTION

Turbulent flow separation continues to be a weak spot for Computational Fluid Dynamics (CFD) due to its highly unpredictable nature, especially around the edges of the flight envelope [11]. This includes the dynamics occurring around a stalling wing. The High-Lift Common Research Model (CRM-HL) ecosystem addresses these challenges through a coordinated effort that links computational and experimental teams [12]. Each approach informs the other, aiming to improve both accuracy and collective precision. As computational methods continue to advance, the need for high quality, repeatable experimental data grows stronger. The development of accurate CFD models, specially for complex high-lift flows, counts on experimental data that is reliable and free from facility-specific artifacts so it can be compared to other facilities and simulations. In wind tunnel testing, the integrity of the flow is essential; poor inflow uniformity, wall interference, or any surface irregularity can distort the results and make it difficult to validate simulations or compare across facilities studying the same flows. With plans for experimental testing of a half-span CRM-HL at the Kirsten Wind Tunnel (KWT), an initial phase of the broader effort has involved ensuring that the exploration of high-lift dynamics and sensitivities is independent of wind tunnel specific artifacts or of the integration of the model to the tunnel itself. To achieve this, highly repeatable and reliable integration into the tunnel must be obtained. A well characterized boundary layer is needed to obtain the half-span's symmetry plane [13] and for high quality flow experiments. Which may not be the case in wind tunnel boundary layers due to the odd behaviors present due to the influence of the circuit and contraction. For this purpose, the main objective of this thesis is to design a splitter plate for the KWT's side wall for half-span model testing; creating a uniform, constant pressure flow and a well characterized,

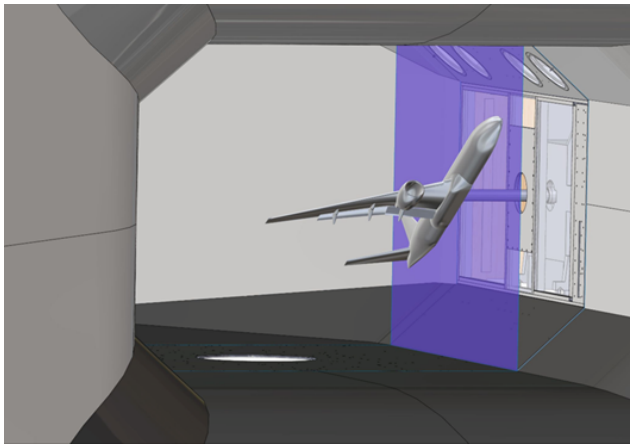

Figure 1.1: Render of a Splitter Plate Mounted over the West Wall of the KWT.

canonical boundary layer.

At the University of Washington (UW), the KWT has been a longstanding facility for high-quality aerodynamic testing. The KWT is a closed circuit, low speed wind tunnel with a rectangular test section and double return, widely used for academic and industrial projects [5]. Still, the KWT does not necessarily have canonical wall boundary layers. The sidewalls of the test section feature chamfered edges which limit the space for high angle of attack (AoA) changes, and can create distortions in the flow near the wall. The actual boundary layer profile along the wall has not been comprehensively characterized, introducing uncertainty into tests involving near-wall flow or wall mounted models. To improve this, the proposal is to install a splitter plate system mounted by the west wall of the tunnel's test section. This plate will be set where the chamfers end, creating a flat, instrumented surface that will work as a well-defined testing base. In doing so, it allows for improved boundary layer control and characterization, higher test angles of attack, and the development of a repeatable, canonical boundary layer. Figure 1.1 shows a render of the plate chosen for the splitter plate, including the KWT's test section with the chamfers and original sidewall balance.

The CRM-HL ecosystem is part of a broader NASA-led initiative supporting the CFD 2030 goals, which call for major advances in CFD's predictive capabilities, particularly in

Figure 1.2: High Lift CRM installed in the 14x22 foot subsonic tunnel at NASA Langley Research Center [1]

complex flow regimes such as separated, unsteady, and turbulent flows [11]. A central objective within this ecosystem is the integration of computational efforts with precise, reliable experimental data. This demands experiments that meet high standards of quality, characterized by low uncertainty, detailed flow documentation, and repeatability across runs and facilities. In this context, a high-quality wind tunnel test is defined by controlled, well-characterized inflow conditions; high-resolution and accurate measurements of surface pressures and boundary layers; and geometries that remain flat and structurally stable under load. As outlined by Oberkampf and Smith [14], six key attributes define a validation-quality experiment: Experimental Facility, Analog Instrumentation and Signal Processing, Boundary and Initial Conditions, Fluid and Material Properties, Test Conditions, and Measurement of System Responses. Meeting these criteria becomes even more critical when testing half-span models, which inherently interact with the tunnel wall and are more sensitive to boundary layer quality, angle of attack variations, and installation repeatability. This is the case for the CRM-HL model discussed here; an example of the half-span configuration is shown in Figure 1.2.

Half-span models offer an efficient way to study complex aircraft flows at higher Reynolds numbers than used with full-span models, while reducing cost and structural complexity [13]. However, integrating them into wind tunnels presents unique challenges, particularly regarding the manner in which the model's symmetry plane interfaces with the wall or surface it is mounted to, and how the boundary layer on that surface is managed. Several methods exist to address these issues, each with trade-offs for testability and manufacture. A common and simple approach is to mount the model directly onto the wind tunnel's surface, accepting the boundary layer as-is. While simple to implement, this leads to higher uncertainty since the boundary layers often might not be canonical, three-dimensional turbulent structures like horseshoe vortices might appear, and conditions vary across facilities. To improve this, some facilities use boundary layer suction along the wall, pulling low momentum fluid towards the surface to thin the boundary layer [15]. While effective, these systems can be complex, require high flow rates, and introduce their own uncertainty as the boundary layer is still recovering when it encounters the test article. Another method to address the wall interference is the use of a peniche, which is a short fairing installed between the model and the wall to simulate a fuselage-like separation and reduce the effect of the boundary layer on the relevant part of the model [16]. Studies suggest the peniche's height can be two-to-three times the displacement thickness of the boundary layer [13]. Peniches can be metric -instrumented to measure loads- or non-metric -used simply to offset geometry-. Metric peniches offer direct load data from the model, but they introduce complexity in design, manufacturing and calibrations. On the other hand, non-metric versions must be precisely managed to avoid introducing new flow distortions. An alterative method to avoid the distortions to the flow introduced by a peniche is to implement a stand-off gap below the model, which allows the symmetry plane to be free of interference and avoids flow structures that could affect the model's loads [13]. It's been suggested that the standoff's height be scaled to four-to-five times the displacement thickness [13]. This standoff gap would require a brush seal that does not impart its own loads to avoid the flow from impinging on the model from below. Turntables are also used in some setups to allow model rotation through angle of attack sweeps over the exact same

surface. These systems require precise alignment and occupy significant space, and can be avoided by setting up a smooth and flat surface such that the distance under the model remains uniform.

For this project, the chosen approach was to use a splitter plate mounted over the tunnel wall, as a clean and well-characterized base for model integration. The model will be mounted using a variable stand-off gap with a brush seal, allowing for adjustable separation between the model and the plate. The model will be supported by a mounting strut that passes through the splitter plate and connects to the wall's side balance system. The mounting will allow for angle of attack changes, without requiring a turntable. Using a splitter plate simplifies the modeling of the test environment, setting a well-understood boundary layer, improving repeatability and simplifying comparisons with CFD. While a metric peniche could provide direct force measurements, the estimated boundary layer thickness of the splitter plate -which would in turn determine the height of the peniche- is too small for the peniche to be a desirable option. Instead, all loads will be measured with the external side-wall balance system.

Designing and integrating a splitter plate for high-fidelity half-span testing presents several technical challenges that must be addressed to ensure reliable data collection. A primary concern is avoiding significant blockage or disturbances to the test section flow. Since the splitter occupies physical space, it inevitably alters the flow field in its wake; thus, careful design of its geometry—including thickness, leading edge, and support structure—is essential to minimize the chance of wind tunnel diffuser stall. Excessive blockage or poor integration may increase pressure losses and trigger diffuser stall, leading to unsteady flow in the tunnel return, potentially creating a non-uniform inflow to the test section. For this reason, diffuser behavior must be monitored during validation, and corrective measures applied if necessary. Another key challenge lies in the manufacturing of the plate itself. The splitter's large size requires the use of large tooling which typically comes with relatively poor tolerances. At the same time, the design demands small, precise features on these large components. Balancing these competing requirements is critical. Choosing different manufacturing techniques based

on the tolerance and quality needs of each piece, and processing key parts in-house for better control, increases the likelihood of producing an accurate and reliable final assembly.

The goal of the splitter is to generate a clean, canonical boundary layer with minimal pressure gradients; this concept will be defined in the background section. Local geometric imperfections or flow misalignments can introduce pressure gradients or non-uniformities. To detect these, pressure taps and boundary layer probes are integrated into the system, allowing for corrective adjustments. As the boundary layer develops along the plate, its interaction with the model becomes increasingly significant. If it thickens too much before reaching the model's leading edge, it can induce separation or alter lift. To mitigate this, the model is positioned downstream of the plate's leading edge, and a stand-off gap is used to reduce interference. Maintaining consistent spacing between the model and splitter is essential—deflections or deformations during testing could introduce variability or even contact the model. A robust support structure and strict flatness validation are therefore required. The leading edge of the splitter must promote uniform flow; a blunt profile could generate local acceleration, lift, or separation, especially at higher angles of attack or under slight tunnel angularity. Flow alignment and stagnation point identification will be critical to ensure consistent test conditions. These challenges inform both the design and validation strategy, ensuring the final configuration provides repeatable, high-quality data.

To meet these requirements, this project focuses on designing, fabricating, and validating a splitter plate with a stand off gap and no turntable. The design prioritizes modularity, stiffness, and repeatability to enable effective fabrication and seamless integration into the KWT while minimizing impact on the baseline flow. The splitter's construction in multiple large sections facilitates transport, installation, and alignment, with additional measures planned to ensure dimensional accuracy and structural integrity. The system incorporates features such as static pressure taps, boundary layer probe access, and a rounded leading edge to promote smooth inflow and flow control. Validation tests including boundary layer profiling and diffuser performance assessment will confirm that the splitter establishes the desired canonical boundary layer without compromising tunnel flow. Overall, this work aims

to deliver reliable, high quality flow conditions for CRM-HL testing, supporting broader efforts to unify computational and experimental aerodynamics research.

Chapter 2

BACKGROUND

2.1 Boundary layers and their properties

Boundary layers form when a fluid flows past a surface, causing the velocity to drop from the free-stream value to zero at the wall due to viscous effects, creating a thin region of velocity gradient near the surface [17] [18]. The boundary layer then defines the shape of the object and how the fluid interacts with it. The boundary layer thickness - usually denoted by δ- marks the distance from the wall where the flow velocities reach approximately 99% of the free stream value. While δ is commonly used, it lacks a sharp definition due to the gradual asymptotic approach to free stream conditions. More robust parameters include the displacement thickness, δ^*, which quantifies the reduction in flow area due to the boundary layer (expressed with Eq.2.1), and the momentum thickness, θ, which represents the loss in momentum flux caused by the velocity deficit near the wall (expressed with Eq. 2.2). These quantities are useful for analyzing how much the flow is altered by the boundary layer's presence.

$$\delta^* = \int_0^\infty (1 - \frac{u}{U})dy \tag{2.1}$$

$$\theta = \int_0^\delta \frac{u}{U}(1 - \frac{u}{U})dy \tag{2.2}$$

Boundary layers can exist in either laminar or turbulent states, each with distinct characteristics. The Reynolds number provides a useful indicator for the likely state of the boundary layer, but the distinction between laminar and turbulent flows lies in their fundamental behavior. In laminar boundary layers, the flow is smooth and orderly, with streamlines moving in parallel and a steady deceleration of the velocity from the free stream to the wall. In

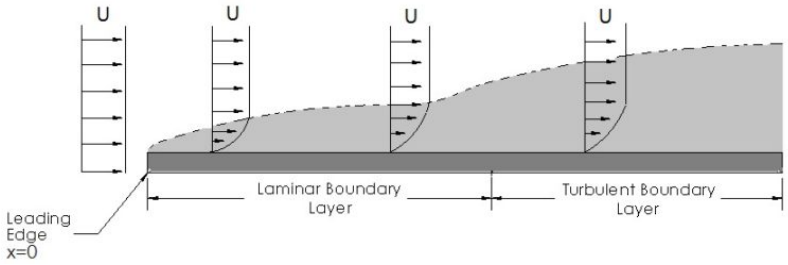

Figure 2.1: Canonical Boundary Layer - Laminar and Turbulent [2]

contrast, turbulent boundary layers are unsteady and chaotic, with fluctuating velocity components and enhanced mixing. In this regime, the wall shear that drives the boundary layer also supplies energy to sustain the turbulence [19]. Figure 2.1 shows an ideal representation of a laminar boundary layer transitioning to turbulent.

A canonical boundary layer is an idealized model used to study boundary layer behavior in a simplified, replicable context. Specifically, a turbulent canonical boundary layer refers to flow over a flat plate with a zero pressure gradient and sufficiently high Reynolds number such that the flow is fully turbulent and no longer influenced by the transition process. Importantly, a canonical boundary layer is independent of the conditions upstream, meaning it is not affected by the initial turbulence, pressure gradients or tripping devices and so, the plate must be long enough for the flow to forget those initial conditions. Turbulent boundary layers are typically divided into regions where different physical mechanisms dominate the momentum transfer. These regions appear naturally from a classical dimensional analysis of the governing equations. Close to the wall, the only relevant velocity and length scales are the friction velocity u_τ, which is derived from the wall shear stress and the viscous length scale ν/u_τ; where ν is the kinematic viscosity. This defines the inner layer, where the flow is dominated by viscous effects and the velocity increases linearly with the normalized distance from the wall. This region is often referred to as the viscous sublayer, and its velocity profile can be described by Eq.2.3.

$$u^+ = y^+ \tag{2.3}$$

$$with : u^+ = \frac{u}{u_\tau}; \tag{2.4}$$

$$y^+ = \frac{yu_\tau}{\nu} \tag{2.5}$$

As the distance from the wall increases, inertial and turbulent effects grow more relevant while viscosity becomes negligible. In this region, the relevant velocity scale remains u_τ, but the characteristic length scale becomes the wall-normal distance y, leading to the classical logarithmic velocity profile described by 2.6, where κ is the von Kármán constant, and B is an empirical constant. The region where this holds is known as the log layer or law of the wall region. Between these two layers lies a buffer region, a transitional zone where both viscous and turbulent stresses are important but not easily modeled by one single expression.

$$u^+ = \frac{1}{\kappa} ln(y^+) + B \tag{2.6}$$

The law of the wall region behaves in inner and outer variables, leading to two possible scalings. Near the wall scaling, the log law is non-dimensionalized using Eqs. 2.5 and 2.4: the inner units or variables. For the outer variables, the scaling is done with freestream velocity, given this is dominated by large-scale turbulent motions. For these, the wall normal coordinate and velocity scaling in Eqs. 2.7 and 2.8 are used; where U_e is the velocity at the edge of the boundary layer.

$$\eta = \frac{y}{\delta} \tag{2.7}$$

$$\frac{u(y)}{U_e} \tag{2.8}$$

Thus, the velocity profile is often expressed using Coles' composite profile [20], shown in Eq.2.9. Where the profile is composed of the inner log layer and the outer wake region. With Π being the wake strength parameter and $W(\eta)$ is the wake function.

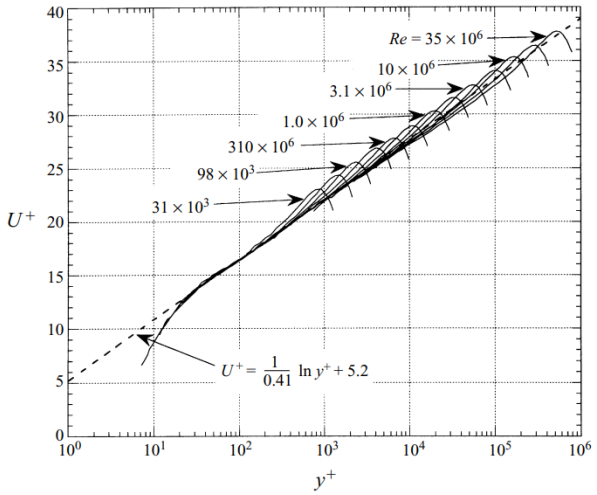

Figure 2.2: Velocity profiles normalized using inner scaling variables [3].

$$\frac{u}{U_e} = \underbrace{\frac{1}{\kappa} \ln y^+ + B}_{\text{Inner (log) layer}} + \underbrace{\Pi * W(\eta)}_{\text{Outer wake region}} \tag{2.9}$$

All of these regions are highly influenced by the Reynolds number. The log-law region will need a high Reynolds number to be properly defined and clearly separate the inner and outer behavior. Figure 2.2 shows boundary layer velocity profile results obtained by Zagarola and Smits [3] for 13 different Reynolds numbers between $31x10^3$ and $35x10^6$.

This figure shows the alignment with the log law, using $\kappa = 0.41$ and $B = 5.2$, as well as the deviation towards the outer region. Complementary, Figure 2.3 (a,b) shows the plots of velocity scaled by u_τ and $U_{CL} - \bar{U}$, once again obtained by Zagarola and Smits [3]. The figure shows that when scaled by u_τ, the velocity profiles do not collapse onto a single curve, the way they do for the alternative outer scaling [3]. For both of the scalings, it is noticeable that there is no collapse on the low Reynolds number region, which is to be expected given that this region is not properly defined for $Re < 400x10^3$ [3]. In this region, the difference between velocity scales is more evident, given that at high Reynolds numbers, the scales are proportional.

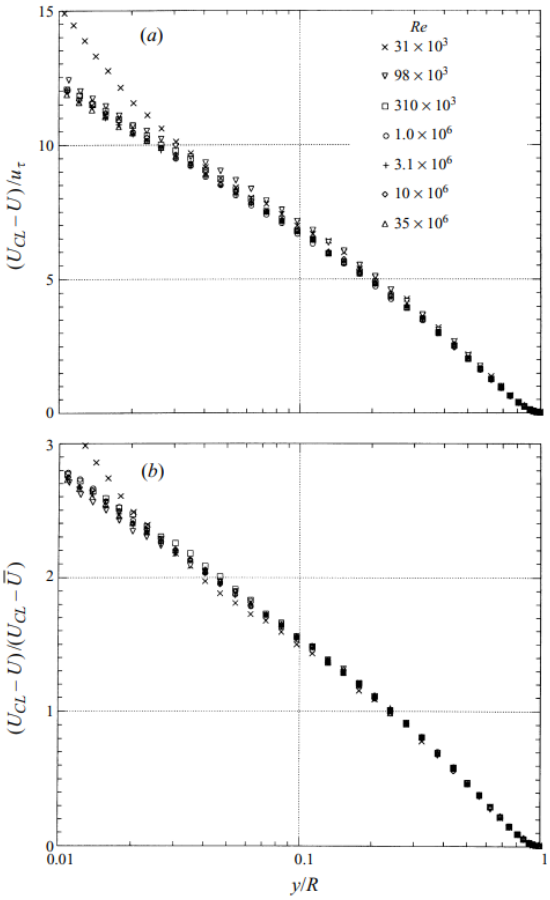

Figure 2.3: Comparison between the velocity profiles normalized by u_τ and $U_{CL} - \bar{U}$ [3].

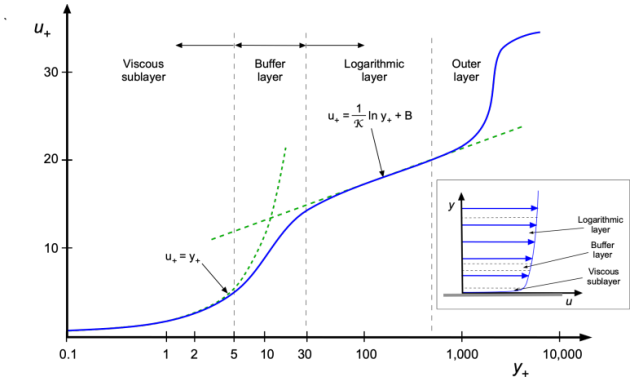

(a) Turbulent Boundary Layer Regions [21]

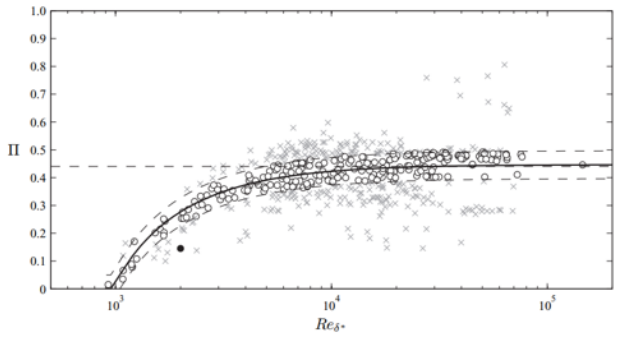

(b) Strength of the wake component vs displacement thickness based Re [22].

Figure 2.4: Turbulent Boundary Layer Regions and Wake component

Farther from the wall, in what is known as the outer layer, the flow becomes increasingly influenced by the overall boundary layer thickness δ, and the velocity profile can be described by the velocity defect law. In this region, the mean velocity approaches the freestream velocity and the turbulent eddies scale with δ rather than the viscous length scale; this outer layer is what is referred to as the wake region. Figure 2.4a illustrates these regions and their associated velocity profiles. It is worth noting that in Figure 2.4a the scale of the wake is bigger than would be expected.

One important parameter for this wake region is the wake strength parameter (Π), which

quantifies the contribution of the wake to the full velocity profile (as seen in Eq.2.9) and represents how strong the deviation is from the log-law region in the outer boundary layer. The structure of this emerging wake is strongly dependent on Reynolds number. As seen in Figure 2.4b the wake strength parameter initially increases with Re_{δ^*}, and reaches a constant value. This relative stability is a sign of a canonical boundary layer [22]. An experimental aspect that can have an impact on this wake component is tripping. This refers to the intentional introduction of surface roughness or disturbances that force a laminar flow to transition to turbulent flow at a specific point [23]. For a well-tripped boundary layer, or one for which the upstream history has been forgotten, the wake strength will have this behavior. If the boundary is not well tripped, the wake region will deviate from the ideal curve shown in Figure2.4b, and the log layer will not be well developed [20]. Conversely, if excessive tripping is introduced -either too early or too aggressively- the boundary layer's natural development can be affected. The log layer may not form properly and the resulting wake structure can be altered. This can lead to non-representative pressure distributions and velocity profiles.

To determine whether a boundary layer is canonical, several key criteria must be assessed, most importantly, the presence of a zero pressure gradient. This can be quantified using a non-dimensional pressure gradient parameter, such as the Clauser pressure gradient parameter [24], defined with Eq.2.10. This parameter compares the strength of the pressure gradient to the viscous forces at the wall.

$$\beta = \frac{\delta^*}{\tau_w}\frac{dP_e}{dx} \tag{2.10}$$

The parameter can fall into one of three categories. For a boundary layer to be considered truly canonical, β must be very close to zero. There is no single threshold for what is considered close enough to zero to fit this category, but various studies will set diverse references. For example, studies by Örlü and Schlatter [25] establish that a zero pressure gradient parameter will have a $\beta < 1x10^{-2}$.

There is a secondary parameter that can help quantify the pressure gradients in boundary

layers and verify the zero pressure gradient condition. This is the acceleration parameter K defined by Eq.2.11; where $\frac{dU_e}{dx}$ is the streamwise gradient of freestream velocity. This parameter characterizes the effect of the streamwise velocity gradients on the boundary layer's behavior [26].

$$K = \frac{\nu}{U_e^2} * \frac{dU_e}{dx} \tag{2.11}$$

Physically, the parameter quantifies the relative strength of the acceleration of the freestream flow. A high value of K will imply a strong acceleration, which tends to suppress turbulence. If K is high enough, this might lead to a process of relaminarization, where a turbulent boundary layer can transition back to a laminar state [26]. Thus, for a zero pressure gradient turbulent boundary layer, K needs to be once again quite close to zero. Studies by Örlü and Schlatter [25] establish the threshold of close enough to zero to be $K < 1.6x10^{-9}$, while Patel [27] sets it at $K < 5x10^{-6}$. These parameters allow the comparison of the experimental results obtained during flow characterization, to verify that the boundary layer meets the standards for a zero pressure gradient.

2.2 Controlling wind tunnel boundary layers to aid repeatable half-model measurements

Using a half-span model in wind tunnel testing requires a different setup than that of a full-span model. Using them has certain advantages: the scaling can be smaller, leading to a bigger model and more detailed features. This also implies that the model can be lighter and less expensive than the full-span at equal scale. By using half-models, wind tunnel testing can go up to approximately double the Reynolds numbers achieved with a full-span [13]. Still, these models pose a different challenge for testing. Given that the symmetry plane of the model is directly where the mounting surface would go, this plane must be as undisturbed as possible. The interactions between this symmetry plane and the tunnel's wall also makes it difficult to obtain accurate and repeatable data that is not linked to the specific facility. A fundamental challenge in creating this accurate and undisturbed symmetry plane is the

mounting surface's boundary layer. Upon direct interaction between the model and the boundary layer, three-dimensional turbulent structures may develop - such as horseshoe or hairpin vortices- which will directly disturb the symmetry plane, affect the loads measured, quality, and how repeatable the tests can be. Given this challenge, there are multiple ways to control these boundary layers that allow the attainment of good load measurements.

The first option consists of mounting the model directly on the tunnel's test section wall. This would initially require a characterization of the boundary layer at the tunnel's mounting wall, to understand the profile of the boundary layer and how high its impact will be on the model. Conventional wind tunnel side wall boundary layers are often thick, turbulent and non-uniform. These characteristics result in a boundary layer with a strong momentum deficit. Given the challenges that arise upon the interaction of the boundary layer and the half-model, this option would require a method for the removal or thinning of the boundary layer. This could be done by using suction of the side wall, commonly used in wind tunnel facilities. Suction uses fine slots or holes on the surface, which remove low momentum fluid near the surface, as can be seen in Figure 2.5a. This stabilizes the boundary layer and can maintain it laminar for a longer period of time [15]. In this particular case, the suction would help thin the boundary layer, reduce the momentum deficit, and restart its development with a thinner internal layer. The effectiveness of this method is subject to the upstream history of the boundary layer. If it is too thick, it will require a much stronger suction over a larger area, and an already turbulent boundary layer will not be as sensitive to the effects of suction. The remaining boundary layer will still be highly perturbed and will not be fully canonical until much further downstream. This once again ties the obtained results to the specific facility, impacting repeatability.

The second option would involve introducing a splitter plate into the wind tunnel. A splitter is a flat, thin plate used to serve as a symmetry plane for half-model testing. This configuration separates the model from the tunnel side wall boundary layer - as seen in Figure 2.5b. It is designed to induce a new boundary layer, reduce the influence of the tunnel's walls on the flow near the model, and overall create a more uniform flow for testing.

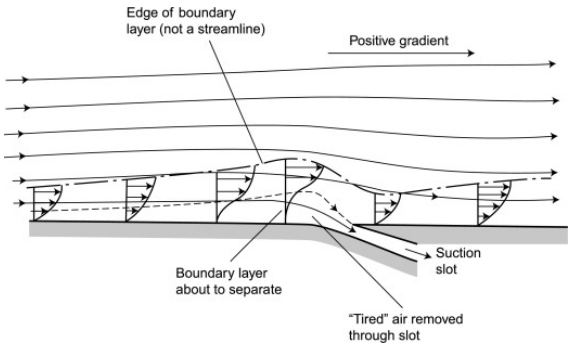

(a) Boundary layer suction [28].

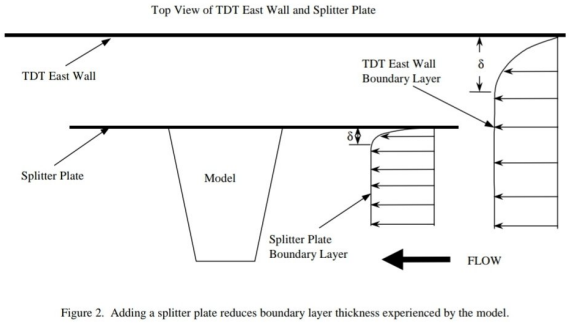

(b) Splitter plate in front of wind tunnel wall for half-model integration [29].

Figure 2.5: Wind Tunnel Boundary Layer Control Methods

As a custom made secondary wall, the splitter can be built to the required dimensions, which is useful for extending the testing base in wind tunnels with chamfered walls. It can also incorporate fully integrated instrumentation, simplifying flow characterization. The splitter introduces its own boundary layer which, although thinner due to its shorter development length before reaching the model, still requires careful control to manage its interaction with the flow around the model. The splitter will also add blockage in the wind tunnel, and might generate non-uniformities in the circuit. If not properly designed, the splitter might shed wake structures that interact with the lower surface of the model, or lead the flow to separate upon contact with the plate. These considerations are to be revised during the design process so the splitter plate can preserve repeatability, but despite these, the splitter remains a widely used approach, offering a more canonical and controlled test environment than direct wall mounting.

2.3 Methods of half-model integration

Independently of whether the half-model is mounted directly onto the tunnel's sidewall with boundary layer control, or onto a splitter plate, it will still require further action to avoid the interactions between the model and the boundary layer of the mounting surface to obtain an undisturbed symmetry plane. An approach to solve this is to displace the model past the boundary layer, leaving a gap between the surface and the model. This solution helps avoid or reduce the interaction between the model and the symmetry plane, but leaves the question of how this gap will be sealed to avoid the flow from going under the model and altering the loads. There are two main approaches to take for this method: the use of a peniche and that of a stand-off gap.

A peniche is a two-dimensional profile extrusion of the model's fuselage, extending from the model's base to the mounting surface, as seen in Figure 2.6a. This non-metric spacer is used to reduce the interference of the boundary layer upon the model's loads. This method helps displace the model beyond the boundary layer and ensures that no airflow is going underneath the model. Still, there are some challenges that come with using this method. Even though the peniche can help reduce the wall's boundary layer's interference, it can increase complexity to the flow field, displace the flow, and contribute additional drag. Given that a body is still in direct interaction with the boundary layer, the peniche has the potential to introduce three-dimensional flow structure that can alter the flow. As suggested by Eder, Hufnagel and Tropea [16], the peniche and its resulting vortices can alter the flow around the model and its effect can be hard to quantify and correct. It is also established in said publication, that peniche height can generate discrepancies between the aerodynamic moments and coefficients -varying with AoA- of the half-span and the full-span. Meaning the symmetry plane would be compromised. The peniche will usually utilize a labyrinth seal, which will increase the complexity of the method, especially in smaller peniches. Another challenge is the need to ensure the peniche is non-metric, so the loads that are exerted on the surface of the peniche are not taken into account for the total measurements of drag and lift

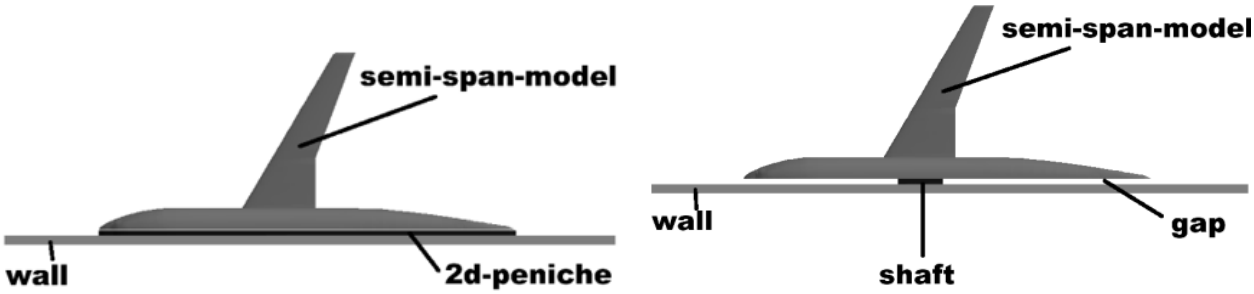

(a) Half-Span Model with Peniche [16]

(b) Half-Span Model with Stand-Off [16]

Figure 2.6: Boundary Layer Control Methods - Displacement

[30]. Finally, there is no single, standardized dimension to use for the height of the peniche that will ensure a proper symmetry plane. As a baseline reference, Skinner and Behtash [13] establish that a standard peniche can be scaled to two to three times the displacement thickness.

A peniche is typically paired with a turntable to seal the gap between the model and the mounting surface, particularly when the model is rotated to different angles of attack. Figure 2.7 shows this circular section beneath the model. The peniche is fixed to the turntable, so when rotation is needed, the entire peniche and turntable assembly rotates together. This not only ensures that the model is sealed, but also provides that while rotating the model will be over the same surface at all times, thus if there are any imperfections in the surface, they won't alter multiple locations and can be isolated. This should not be needed if the surface upon which the model is mounted is smooth and uniform enough. The turntable may also complicate the development of the seal if the model is too big and exceeds the maximum diameter the turntable can have.

The alternative method for displacing the model away from the boundary layer is the use of a well-chosen stand-off gap. As seen in Figure 2.6b, this consists of setting the model at a specific distance away from the surface, avoiding the boundary layer and setting the

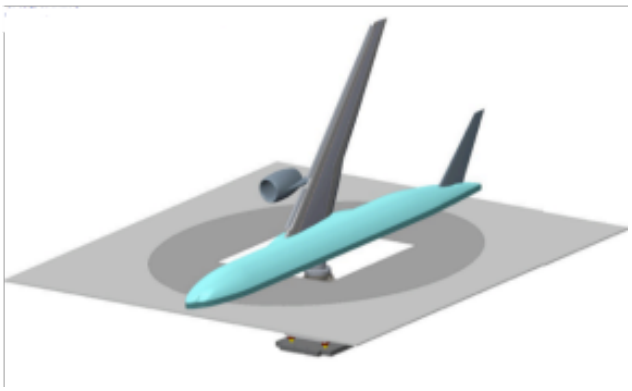

Figure 2.7: Model mounted on turntable [4].

symmetry plane away from any disturbances. This method prevents the introduction of three-dimensional structures due to direct interaction with the boundary layer, and is much simpler in practice. The challenges related to this method would be ensuring that there is still a seal between the model and the surface so the air flowing underneath the model does not impart loads. Additionally, just as with the peniche, there is no one single standardized height for the stand-off gap that ensures loads are robust. Still, as a reference, studies carried out by Skinner and Behtash [13] found that setting a stand-off gap of four to five times the displacement thickness of the boundary layer, can achieve a flow field around the model that represents what would be expected of an equivalent full span model in free-air. Studies by NASA [31] found that half-span models are more sensitive to changes in the standoff height than to variations in the mounting surface's boundary layer; from which it can be seen that the ability to adjust the stand-off distance may be more relevant than a boundary layer with little development over the entire length of the model.

Wind tunnel testing in different facilities can be carried out with multiple combinations of the previous methods for boundary layer management. Most of the time, half-span models are mounted directly onto the tunnel wall or floor -sometimes set on a splitter plate and turntable combination, but aligned with tunnel's surface- which is why the use of a peniche is quite common. A peniche is typically used when the boundary layer, or the distance

between the model and the surface, is at least a few inches thick. When the boundary layer is too thin, especially just a few millimeters, building a functional peniche becomes impractical, particularly due to challenges with sealing elements like the labyrinth seal. For studies carried out by Doerffer and Szulc [30], Mamou and Broughton [32] and Evans et al. [12], a peniche was used to mount the model above the tunnel's boundary layer. In some of these cases, additional methods for control were used such as suction and blowing, reducing the boundary layers from their original thickness. Thus, allowing the integration of a peniche with a height between 3.2-3.7 inches for all three cases.

Chapter 3

FACILITY AND METHODS

3.1 Kirsten Wind Tunnel

The splitter plate was designed for the Kirsten Wind Tunnel (KWT) at the University of Washington. Operational since 1939, the KWT is a subsonic, closed circuit, double return wind tunnel, with a rectangular eight feet high, ten feet long, and twelve feet wide test section, with 45°chamfers in the corners; as seen in Figure 3.1 [5]. For reference, the x-axis spans over the twelve feet width from west to east wall, the y-axis over the ten feet length from beginning to end of the test section, and the z-axis spans the vertical height of the test section. It has a maximum air speed of 90 m/s (200 mph, 100 psf).

Common tests carried out in the KWT include force, pressure and flow visualization. Force tests can use the six-component balance beneath the test section or a side wall balance, pressure tests connect the model's pressure ports to the KWT's electronic pressure scanning (EPS) modules, or pressure transducers. Flow visualization tests are carried out with smoke, china clay, minitufts, among other available methods.

Some of the values being measured in the test section include dynamic pressure, static pressure, temperature, and aerodynamic loads. Dynamic pressure is monitored using differential pressure transducers connected to calibrated pitot probes placed upstream of the model. Static pressure is obtained from the tunnel's dedicated static pressure strip, located on the test section floor, just upstream of the model region. It is important that this static strip not be covered at any point, which limits how far into the upstream region of the test section elements can go. Given the 10' length of the test section, the static strip is set approximately 6" upstream from the start of the test section. This placement provides a representative and minimally disturbed measurement of static pressure in the flow. This

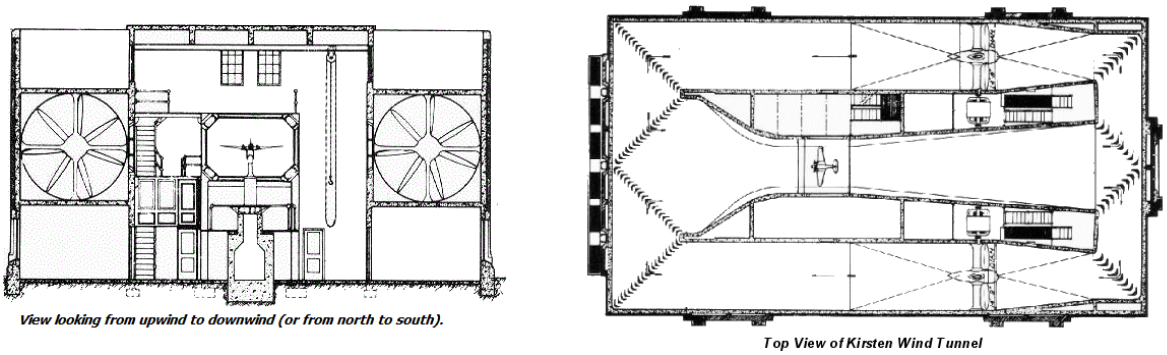

(a) KWT View From Upwind

(b) KWT View From Top

Figure 3.1: Kirsten Wind Tunnel Views [5]

static pressure is measured using a high-accuracy absolute pressure transducer, Omega model PX425-030AV with full-scale range of 0 to 30 psi and an accuracy of $\pm 0.05\%$ of full scale [5]. The test section temperature is recorded using a resistive temperature device (RTD) mounted within the flow path, offering precise temperature data necessary for calculating air properties and Reynolds number. This RTD has a full-scale range of 5 to 300 degree Fahrenheit with an accuracy of ± 1 degree Fahrenheit [5]. Additionally, the six-component main balance measures all forces and moments at the same time, respect to the wind axes at the virtual balance moment center that is in the center of the test section [5]. This data is converted to voltages that are then amplified and converted to digital engineering units.Additionally, a breeze shield protects the balance area from the effects of drafts and near airflow.

The KWT also features an advanced traverse positioning system that enables precise three-dimensional probe placement within the test section -crucial for characterizing uniformity. The system consists of ceiling mounted tracks that allow a motor-driven carriage to move over the x- and y- axes, while two vertical struts on the carriage provide z-axis motion [5]. Each axis is computer-controlled, with a maximum traverse speed of 5 in/s for x and y, and 10 in/s for z, allowing rapid and repeatable scanning paths. By mounting pitot tubes,

hot-wire, or other flow sensors on the struts, the dynamic and static pressure distributions across the section can assess both longitudinal and cross-sectional flow conditions. Overall, the traverse rig serves as a vital tool for facility characterization, enabling rigorous baseline mapping.

The KWT also features a sidewall balance (SWB) that provides high-fidelity six-component force and moment measurements for half-span model configurations. Installed externally to the test section on the west wall, the SWB allows for direct acquisition of aerodynamic loads. The system is calibrated through a series of precision weight applications and moment arms, and its load paths are isolated using aluminum flexures designed for infinite fatigue life. The SWB is capable of measuring lift, drag, and pitching moment with typical full-scale uncertainties under 0.4%, 0.5%, and 0.35% respectively. This level of precision enables the detection of subtle aerodynamic changes in controlled wind tunnel environments, making the system well-suited for sensitive measurements such as those required during splitter plate integration and validation [33]. Its integration with an actuated pitch system, encoder feedback, and a custom mounting interface enables repeatable angle-of-attack sweeps. The capabilities of this balance were validated using a half-model swept-wing mounted on a circular splitter plate -shown on Figure 3.2- as documented in a NASA supported icing effects study [6], where the data quality was shown to compare favorably with results from other major facilities. While the study centered on artificial ice-shape formations, the broader outcome confirmed that the SWB setup is capable of delivering reliable, repeatable aerodynamic data in semi-span configurations.

The flow quality of the KWT has been surveyed periodically through its long lifetime. The airflow in the KWT has a flow angularity of -0.012°in upflow and 0.0°in crossflow [5][7]. Even though the last value reported for turbulence intensity was 0.72% [5], it is suspected that the real current value is lower. A new tunnel qualification is ongoing. In their 1979 report, Shindo and Rae [7] explored flow quality after adjusting the vanes to obtain a more uniform flow in the tunnel circuit. Figure 3.3 shows the comparison for the lateral component of turbulence, upflow and crossflow angularity, before and after the improvements were carried

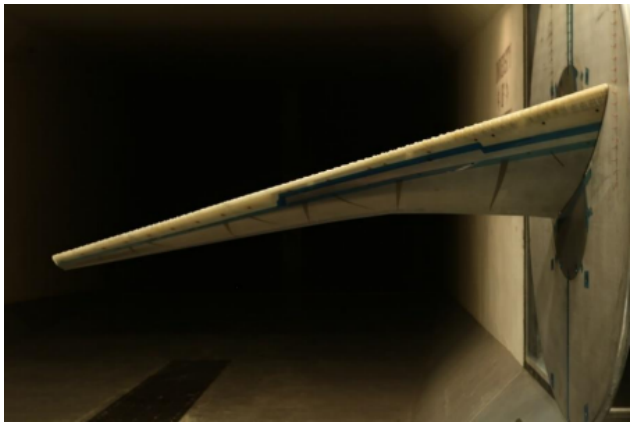

Figure 3.2: Half-model swept-wing mounted on splitter plate and SWB [6].

out. The plots after improvements reflect the values reported for the three parameters, flow angularity of -0.012°in upflow and 0.0°in crossflow and turbulence intensity was 0.72%.

The most recent flow quality assessment was carried out in 2018 by Knowlen and Hudgins [34] which mapped the flow quality at the entrance and mid-plane of the test section and measured the uniformity of the flow at these points. It was found that the average relative deviation in dynamic pressure, q, was 1.61% at the entrance and 1.84% at the center for q = 5 psf, and decreased for q = 50 psf, at 0.44% and 0.69% at the entrance and center respectively. Later in 2019, a brief boundary layer survey was carried out by Stevens [35], which found the boundary layer at the west wall -where models are mounted- to be less than 4.5 inches thick. Thus, it was suggested that the models be placed far enough from the wall to avoid this boundary layer, possibly through longer struts. A new tunnel flow survey is currently underway, aimed at obtaining the following data: wall pressure evolution across all four walls of the test section, side wall boundary layer uniformity, test section mean uniformity, and freestream turbulence levels.

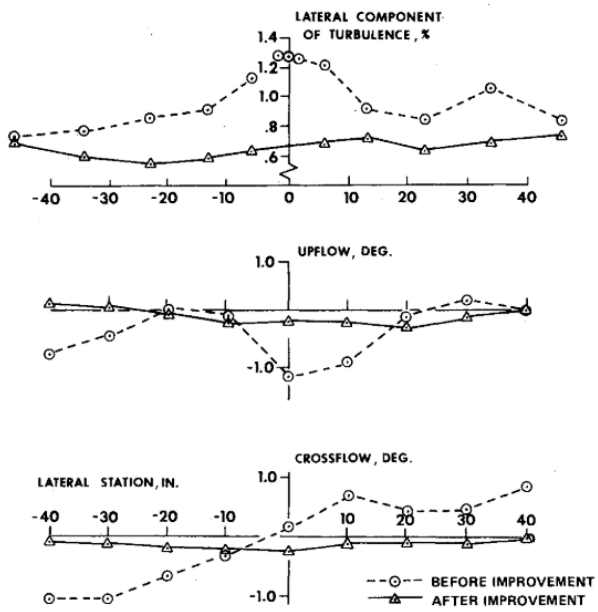

Figure 3.3: Flow characteristics at test section centerline, before and after improvements carried out by Shido and Rae [7].

Chapter 4
SPLITTER PLATE DESIGN

4.1 Requirements

As stated previously, to achieve the goals of the project a splitter plate must be created with an adjustable stand-off gap with a brush seal and no turntable. To guide the design and validation process of the splitter plate, the following base requirements were set:

- The splitter plate must fit in the KWT's test section and avoid the chamfers. The splitter plate must be 8 by 10 feet, covering the entire west wall of the test section, and must be approximately 18" away from the wall to avoid the 45°chamfers at the top and bottom.

- The splitter plate must be flat. Maximum overall deformation must be within 15% of the model's stand off distance.

- The splitter plate must not be overly sensitive to small angle of attack differences or angularity in the tunnel. This helps promote a smooth, attached flow at the plate's nose, and seeks to prevent separation off the leading edge.

- The splitter plate must have a way to adjust its stagnation point if necessary.

- The splitter plate must be designed for easy installation and removal from the tunnel to allow for repeated use.

- All KWT test articles must achieve a factor of safety of at least five.

- The splitter plate's boundary layer must have a zero pressure gradient. This will help ensure that it is canonical. This will be checked by comparing the value of the acceleration parameter K obtained experimentally and that given by Patel [27] of $K < 5x10^{-6}$.

- The splitter plate's boundary layer must have a determinable log-law region, and the wake component must closely follow the expected Reynolds number variation as stated in Coles [20].

4.2 Theoretical calculations of boundary layer thickness development

To support design decisions for the splitter plate, it is useful to have an empirical estimation of the boundary layer development on the plate. For this purpose, the following previously introduced measurements will be obtained: boundary layer thickness, displacement thickness, and momentum thickness - shown previously in Eqs. 2.1 and 2.2.

Estimations of the boundary layer, displacement and momentum thicknesses can be obtained from empirical formulas, Eq.4.1-4.3, respectively [36], assuming the origin of x to be the geometrical leading edge of the splitter plate. The true evolution of these thicknesses will be measured directly after the splitter plate is completed.

$$\frac{\delta}{x} \simeq \frac{0.38}{(Re_x)^{\frac{1}{5}}} \tag{4.1}$$

$$\frac{\delta^*}{x} \simeq \frac{0.048}{(Re_x)^{\frac{1}{5}}} \tag{4.2}$$

$$\frac{\theta}{x} \simeq \frac{0.037}{(Re_x)^{\frac{1}{5}}} \tag{4.3}$$

To estimate the boundary layer development along the splitter plate, these equations are evaluated at four streamwise locations, with respect to a 4% CRM-HL model placed on the splitter plate: beginning of the plate (union between the leading edge and plate), model nose, model's mount location, and model's tail. The estimated thicknesses at each of

Location	x (mm)	Re_x	δ (mm)	δ^* (mm)	θ (mm)
Beginning of LE plate	127.00	7.72 E+05	3.21	0.41	0.31
Nose	437.90	2.66 E+06	8.63	1.09	0.84
Middle	1692.15	1.03 E+07	25.45	3.22	2.48
Tail	2946.91	1.79 E+07	39.67	5.01	3.86

Table 4.1: Estimated boundary layer thicknesses on the splitter plate

these locations can be seen in Table 4.1 and are plotted in Figure 4.1, where the half-model pictured is scaled for the x-axis (distance along the plate) but not for the y-axis and the four locations are marked with vertical orange lines. The case parameters used with a tunnel airspeed of 90 m/s (200 mph), and a model angle of attack of 0°.

The boundary layer is seen to grow by 460% from the nose to the tail. A significant growth in boundary layers can displace the external flow, modifying the local pressure distribution. It is not ideal to have the boundary layer grow almost five times from the nose to the tail of the model, and this will need to be accounted for with the brush seal as well as when selecting and modifying the standoff distance.

Given that the stand-off can be scaled as four-to-five times the displacement thickness as mentioned previously [13], this empirical data will allow the estimation of a baseline stand-off height. This value will be a reference when examining the splitter's flatness as stated in the requirements. Given the growth of the boundary layer, this height was estimated with the third location -middle of the model- as an average. Thus, the found baseline stand-off gap will be 12.88 mm (0.51 in) which corresponds to four times the displacement thickness at the middle of the model (3.22 mm).

4.3 Philosophy

A design project of this magnitude comes with several challenges,such as the large size of the splitter plate— 8-by-10 foot —which requires high-dimension stock and large-scale

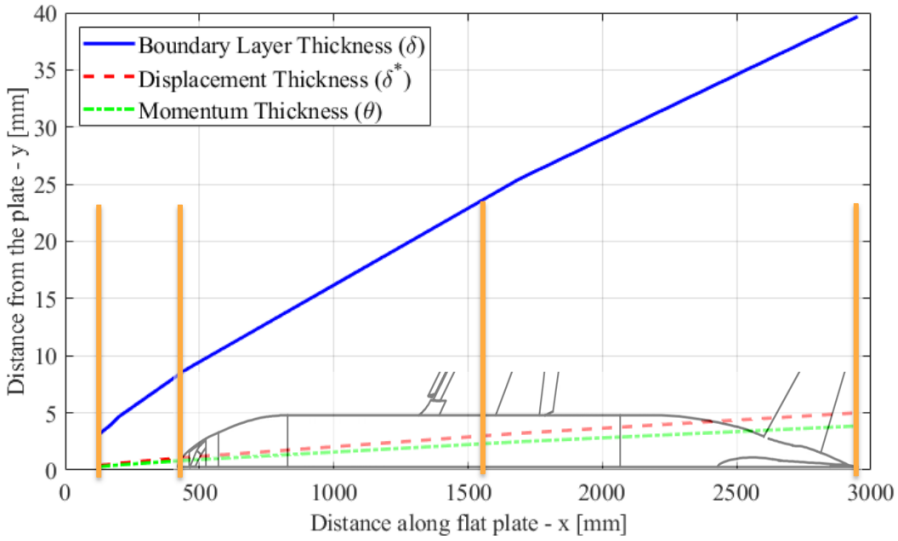

Figure 4.1: Empirical boundary layer thickness, displacement thickness and momentum thickness development over half-span sketch.

machining. However, both large raw materials and oversized machines often come with poor tolerances. As a result, any small or precision features must be carefully evaluated to ensure the manufacturing tolerances align with the functional requirements of each element. The dimensions needed for the pieces will also limit the availability of commercially obtained elements that need very specific geometries, as is the case with the leading edge. The splitter plate's influence on the test section and diffuser is a key concern, as introducing a large surface into the flow will inevitably affect tunnel performance. For this reason, blockage below the plate must be minimized as much as possible, and precautions should be taken around the possibility of generating stall in the diffuser. While blockage could force the flow above the plate to accelerate, generate vortex shedding around the wake region, and alter pressure gradients, diffuser stall could lead to non-uniformities in the tunnel circuit due to asymmetric pressure recovery.

To address the concern of tolerances and overall splitter dimensions, multiple design decisions were made. First off, the body would be divided up into multiple parts that would

then be joined together, breaking down the final size to more manageable dimensions. With this in mind, so flatness is not solely relying on the tolerance of the stock material, structural channels are used to keep the plates flat. In turn, these channels can be shimmed as needed to ensure a proper alignment and no steps between the plates. On the other hand, the machine large enough to process the individual plates (∼39"x96") was a router table, with a tolerance of 0.030". Given that multiple features in the splitter require a smaller tolerance - including small drilled holes, pocket and insert pairs, and features with very high tolerance positioning (approximately ± 0.03") - not everything could be done by the same process. Thus, only some features will be router cut initially. Once those cuts are complete, the remaining components can be manufactured based on measured dimensions of the plates. This includes making inserts after the pockets are cut ensuring they match the real geometry and meet a tighter fit, drilling small holes manually using a magnetic chuck, as well as any holes that require precise positioning.

Following along this line, another design consideration involves the number of fasteners required to hold the splitter together. Regardless of the specific number, a high quantity of bolts will be fastened to the splitter, and must be processed carefully to avoid disturbances in the flow due to their presence. For this purpose, all bolts on the splitter's surface will be countersunk bolts, with a controlled depth (drilled in-house to ensure flush with surface). All the fasteners will be taped over with aluminum speed tape. This same covering process will be done over the seams between elements as well, preventing disturbances as well as air leakage.

One of the pieces that required very specific geometry to meet the design requirements was the leading edge. Given the need for a rounded edge that was proportional to the thickness of the plate itself, most commercial options were not a good fit for the project; for example extruded aluminum airfoils with standard profiles which tend to be broader than the plate. For this reason, a custom 3D printed leading edge, divided onto many independent pieces, would be the solution.

To minimize the chance of diffuser stall, the structural frames were oriented in a stream-

wise direction to reduce the perpendicular area exposed to the flow. Cutouts were incorporated throughout the structures, to reduce blockage, reduce weight, and allow access behind the plate for setup and necessary adjustments. The addition of the trailing edge flap will also allow the stagnation point on the leading edge to be adjusted to account for below-plate blockage.

4.4 Design and Manufacture

The splitter plate design consists of three main body panels, a leading edge or nose, a trailing edge flap, and a system of frames for support, as can be seen in Figures 4.2a and 4.2b.

4.4.1 Plates

The splitter's body is made out of three 39" x 95.625", 3/8" thick 6061 aluminum plates. The plates are joined along their long edges and pulled flat using a series of vertically oriented C-channels positioned along the joint. A row of bolts is set one inch from the edge of each plate and threaded into the C-channels. To bring the plates tightly together, the bolt spacing within the channels is made undersized by 40 thousandths of an inch—resulting in a 1.96-inch spacing instead of the 2-inch spacing on the plates. This undersizing was set taking into account the nominal size of the 1/4-20 bolts to be used, and that of the drilled and tapped holes on the channels and the splitter. A physical prototype was made with different undersizings and then verified with a feeler gauge to select this spacing. This can be seen in Figure 4.3. These unions will be shimmed as necessary to ensure the plates' surfaces are aligned.

Figure 4.4 shows the three plates mounted together, the airflow coming in from the right side. Thus, the plates are referred to as Leading Edge, Middle and Trailing Edge sections from right to left. The splitter has a large number of bolts (around 200) which, as mentioned previously, may create interferences on the surface - all bolts have been marked on Figure 4.4, in blue. For this reason, all of them will be countersunk, to a depth where the head of the fastener is flush with the surface. Given the splitter plate can have an angle of attack,

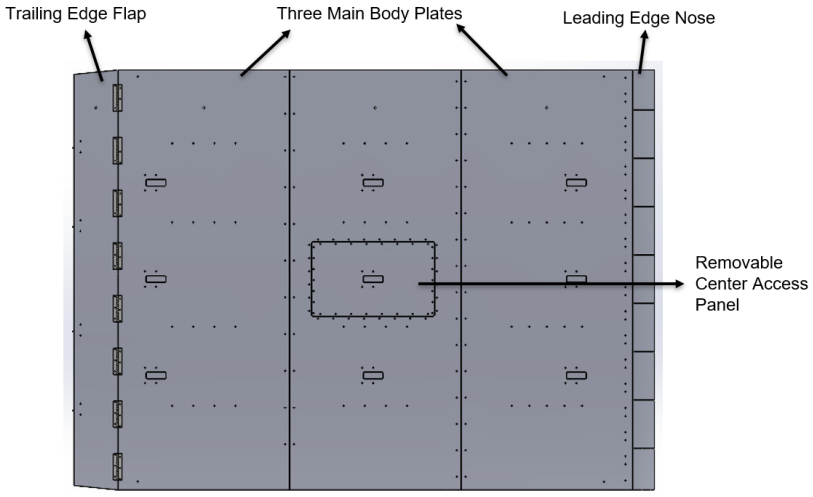

(a) Top view of the splitter plate

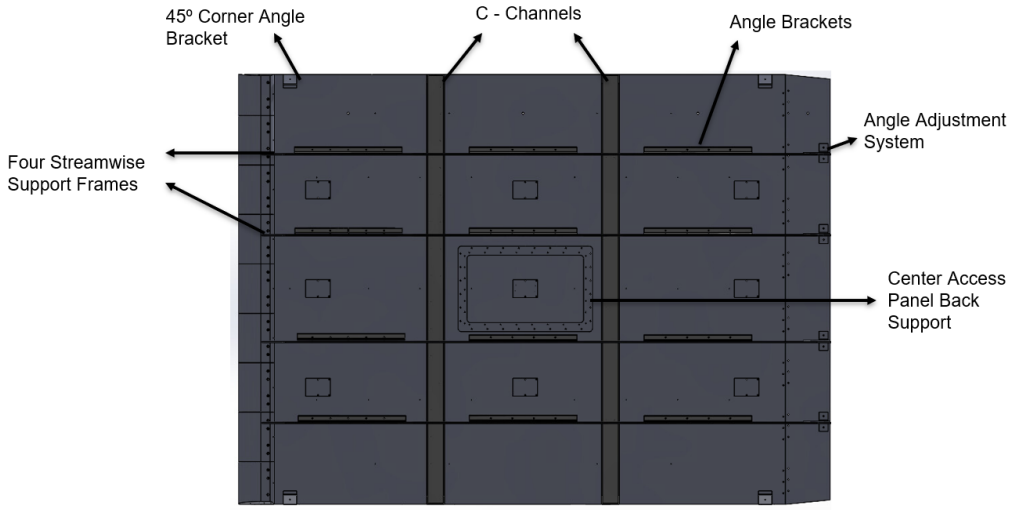

(b) Back view of the splitter plate

Figure 4.2: CAD views of splitter plate system

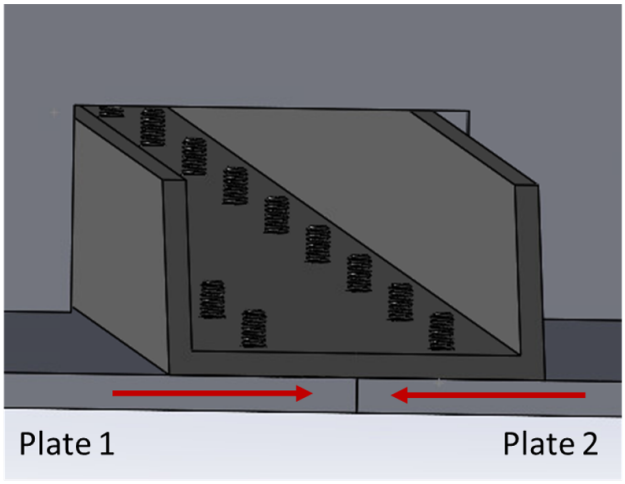

Figure 4.3: C-Channels at union of the plates.

the greater this is, the more it will send a greater load distribution towards the leading edge. For this reason the channel joining the middle and leading edge plate has a greater quantity of bolts than the one securing the middle and trailing edge plates - 32 bolts, in comparison to the 24 found on the latter. This increased quantity of bolts on the leading edge plate will be consistent for all structural features.

The dimensions of each of the plates will come together to form a 117-by-96 inch body. While the sidewall itself has a length of 120 inches, the space the plate can cover is determined by the placement of the tunnel's static pressure strip. This is placed six inches in front of the 120 inch mark, and the splitter plate can come at most four inches over the 120 inch mark, so it does not interfere with the strip. Taking into account the additional length of the leading edge nose, this lines up with the plates' length and any further extension will be found on the trailing edge side. The installed plates will rest uniformly on the floor of the test section. The height of the plate is 3/8" less than the test section to aid with installation. The gap between this upper edge and the ceiling will be covered with aluminum speed tape to create a seal between the two surfaces.

The plates are instrumented with a series of 32 static pressure taps and nine boundary

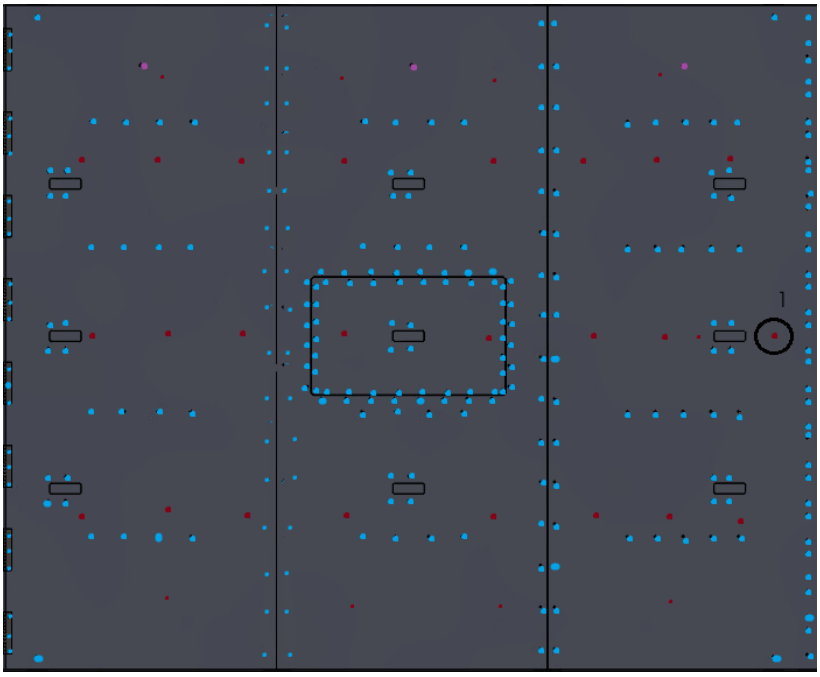

Figure 4.4: Features on the splitter plate body. Markings: Bolts in blue, pressure taps in red

layer measurement locations. The pressure taps are distributed in five rows across the plates: two rows of four taps near the top and bottom edges, and three rows of eight taps—one along the centerline of the plate, and the other two positioned one-quarter of the total height above and below the centerline. The positions of these taps on the plates are marked in red on Figure 4.4. These taps are 1/32" on the front side of the splitter and transition to 1/16" on the back where 90°pressure taps (Scanni 5866-06) will be press fitted and will measure the static pressure as mentioned in the previous chapter. Given that the dimensions of these holes would not be possible to make with the router table and its tolerances, the positions of these 32 taps will be marked by the router table, with a center drill at a controlled depth, on the back of the plates. Following this, the taps themselves will be drilled and reamed in-house for better tolerances for a press fit.

The plates have nine cutouts where a pitot-traverse system can be inserted to measure

the plate's boundary layer to ensure spanwise uniformity and verify displacement and momentum thicknesses. There are three insert pockets per plate, on the centerline, and 20" above and below it; the locations on the x-axis correspond to those of the earlier theoretical calculations and approximately the nose, center and tail of a 4% CRM-HL model. The top-center traverse insert has been highlighted in green in Figure 4.4 for reference. The pitot-traverse will be placed in one of these locations at a time, and the other cutouts will be covered with flat inserts to maintain the smoothness of the surface. Given the required tolerance for a free/close running fit (hole approximately five-thou bigger than the piece), both the pocket and the insert cannot be done with the same tolerance provided by the vendor (30-thousandths of an inch). For this reason once the plates with the cut pockets are obtained, true dimensions will be checked and the inserts will be 3D-printed with the needed tolerances. Details of this pitot-traverse will be discussed in Chapter 5.

Each of the three plates will have a side mount hoist ring (D-Ring) centered at the top of the plate to use as an anchor point for the KWT's crane (each with a vertical capacity of 1,800 lbs). The locations of these mounting points are marked in pink at the top of the plates in Figure 4.4. These will assist the safe and easy mobilization of each of the plates into the tunnel, and later on with bringing them upright into position securely. When not in use, the holes made for these anchors will be covered with grub screws.

To provide an easier access behind the middle plate, a removable access panel was added in the center of the splitter. This 28" x 17", 3/8" thick 6061 aluminum piece can be bolted and threaded onto the main splitter plate and a support frame on the back and removed as needed to access the backside. The dimensions of the panel were chosen to span as much as possible of the center plate without interfering with any of the structural bolts. Initially, this access panel will have only a traverse-pitot insert cutout in the center. Multiple access panels can be made for specific tests to accommodate the necessary model mount, be it a full half model or wing-only model. On that note, while the traverse locations on the center plate will be accessible through this panel, the ones on the exterior plates will be accessible from the sides, between the structural frames.

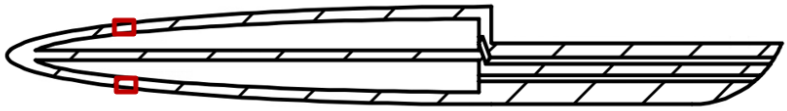

Figure 4.5: Leading edge nose interior profile.

Installation order-of-operations was a critical design consideration for this plate, due to limited access to the backside of the plate when installed. For this reason the bolts fastening the plate to the channels as well as those for the brackets on the structural frames (talked in depth in a latter subsection) and those of the center access panel will be threaded. The bolts fastening the leading edge, trailing edge, and traverse inserts will have nuts on the back of the plate. Once the pieces are joined together, a flatness verification will be carried out and shimming would be done based on need afterwards.

4.4.2 Leading Edge

The leading edge of the splitter consists of a 5:1 rounded fused deposition modeling (FDM) 3D-printed nose, featuring a 3/8" wide cut to create a lap joint with the leading edge plate. The nose will cover the same 95.625" height as the plates and will be composed of nine separate pieces, due to printing height limits. The top and bottom pieces will be 9.125" and 9.5" long respectively, and include 45°miter cut to accommodate the tunnel's chamfers at the top and bottom. The remaining seven pieces are 11" long each and are identical. Pressure taps are placed along their length, be it the 11" or 9.125"-9.5".

Each piece contains two separate cavities—top and bottom—positioned near the leading edge and sealed at the top and bottom. This can be seen in Figure 4.5. These cavities are designed to capture the pressure difference between the top and bottom surfaces of the leading edge. A set of four pressure taps (or three in the shorter top and bottom pieces), each with a 1/32" diameter, is placed along both cavities. These allow the chambers to fill with air and, once the pressure stabilizes, direct flow into the instrumentation system for

Figure 4.6: Leading edge nose mounted on trailing edge plate.

measurement. A pair of 1/16” channels guide each of the cavities towards an external port at the back end of the nose, where metal tubes of that outer diameter are epoxied to make the connection to the pressure tubing simpler.

In order to fit the nine separate pieces together, each of these will have a set of cutouts made at the edges to fit six 3/32” dowel pins on each side. These 1-inch-long dowel pins will be inserted approximately half an inch into each adjoining piece, secured with epoxy, and then the pieces will be pressed together. The same two-part epoxy will be used to coat the mating surfaces to secure the union. The now assembled nose will then be attached to the leading edge plate with bolts and a captured nut on the backside to prevent interferences with the flow. Figure 4.6 shows the joined leading edge nose mounted on the trailing edge plate; the figure is rotated in such a way that the airflow would be coming from the top, towards the bottom of the page.

4.4.3 Trailing Edge

A trailing edge flap is added to the plate to ensure that the leading edge stagnation point can be adjusted with a range from -3°to 10°. This flap is 10” in width, following the end of the trailing edge plate, with the same height as the plates and will have diagonal cuts removing 1” towards the edges of the flap to avoid clashing with the test section chamfers when adjusted to negative angles. The flap will be attached to the trailing edge plate with a series of eight equally spaced 6” hinges. The overall geometry of the flap can be seen in Figure 4.7; this image is rotated in such a way that the airflow would be coming from the top, towards the bottom of the page.

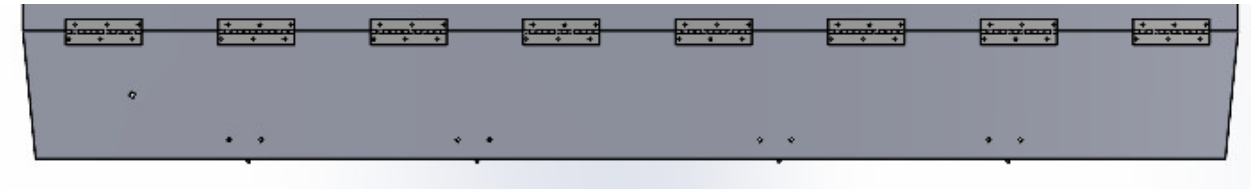

Figure 4.7: Trailing edge flap.

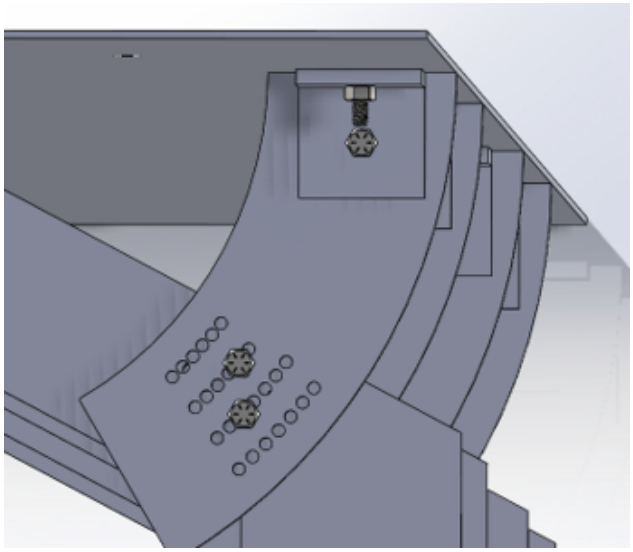

Figure 4.8: Quarter-wheel vernier pin-and-hole angle adjustment system - top view.

To adjust the flap angle as-needed, a quarter-wheel vernier pin-and-hole adjustment system is attached to the flap. The wheel has a set of 26 holes for 10-32 screws, where each hole alignment allows the displacement of the flap by 0.5°for the established range. This system can be seen in Figure 4.8. The position will then be set by securing the wheel to the corresponding support frame with two bolts - the frame system will be detailed fully in the coming subsection, including the connection with this feature. Four of these scaling wheels are used to adjust the entire flap. While in use on the tunnel, the flap angle will be verified using an angle gauge. For this angle adjustment system, it is not critical to obtain the exact angle within the range given. Rather to attain a repeatable position, close to said angle.

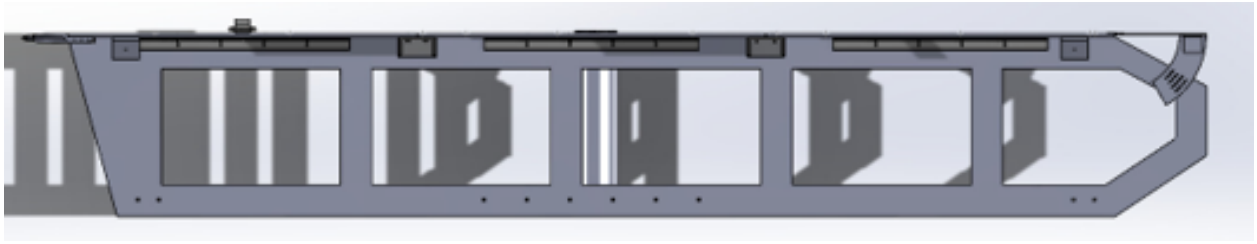

Figure 4.9: Top view of streamwise stringers-frames.

4.4.4 Support Frames

The splitter plate is assembled and supported by the previously mentioned channels, which pull the plates together and keep them flat, along with a set of four horizontal stringers that secure the plate to the tunnel wall. These stringers span the 10 ft test section and are 18" wide, bridging the gap between the splitter—positioned at the chamfer edges—and the tunnel wall. Cutouts reduce mass, minimize blockage behind the plate, and improve access to its back. Three cutouts at the splitter–frame interface are shaped to fit around the two sets of connecting channels and the nose, avoiding interference. The geometry of these frames can be seen in Figure 4.9.

Two of the stringers are positioned at the edge of the chamfers - at the top and bottom - and two are placed 17.75" inward from these locations, towards the center of the plates but still leaving sufficient room for the cutout in the middle plate. Each stringer will be fastened to the splitter using three 2' long angle brackets - one centered on each of the three plates. The locations of these brackets are marked in red on Figure 4.10. The brackets will be secured to the frame with lock washers and nuts. These brackets are threaded on the side facing the plates to allow the plates to be bolted in from the front. As mentioned previously for the channels, the brackets bolted on the leading edge plate will have a greater number of bolts than the two other plates, to strengthen the union considering higher load concentration. Calculations for these fasteners are discussed in Sec.4.6.

On the tunnel wall side, three angle brackets also secure each frame. A 2' long bracket

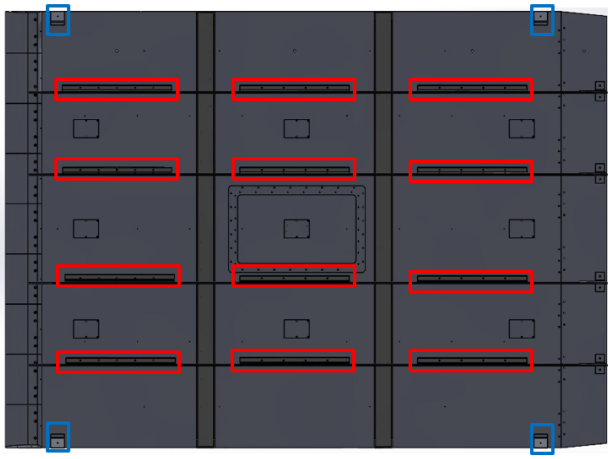

Figure 4.10: Back view of splitter plate with support brackets marked.

will be positioned at the center, aligned with the central bracket on the splitter side, while two shorter 6" will be placed at the sides. The reason for these shorter angle brackets on the sides is the possible threading material on the tunnel wall. As seen on Figure 4.11, there are two plexiglass windows on the sides of the central metal panel onto which the two-foot brackets are threaded into. Wanting to bolt these frames onto either steel or aluminum due to strength and practicality, these sections were avoided and the brackets pushed to the sides. Figure 4.11 marks the mounting locations on the wall; the tabulated fastener locations for the wall can also be found in the appendices. As before, the brackets will be secured to the frames with lock washers and nuts. Bolts will pass through and thread directly into the tunnel wall. In addition to the primary frame structures, 45°angle brackets are mounted at each of the splitter's corners, where it meets the chamfer. These brackets are bolted into the tunnel chamfers to help the splitter maintain its flatness. These brackets are marked in blue in Figure 4.10.

Each frame will include one of the previously described angle adjustment systems for the flap, positioned using two sets of four router-cut holes aligned with the flap angle adjustment locations. For each flap setting, two holes on the quarter-wheel align with two of the eight

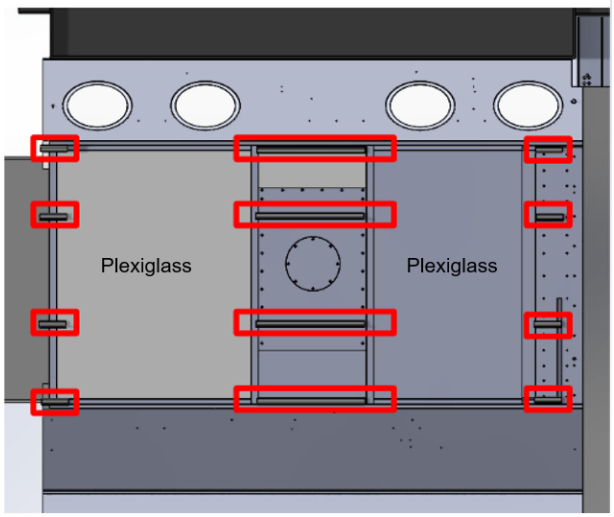

Figure 4.11: Side wall mounting locations.

holes on the frame, allowing the assembly to be securely fastened in place. The assembly of these two parts can be seen in Figure 4.8.

Several manufacturing challenges were identified for these components, the most critical being their overall size. This scale imposed limitations on the selection of fabrication processes and the achievable tolerances, particularly for the largest parts. Since large stock materials and machinery tend to produce greater dimensional variability, it was determined that the three main body plates must be manufactured first, so they can serve as the reference geometry for all other components. Once these plates are received, all secondary parts - such as brackets, channels, and inserts- will be adjusted and aligned based on the actual dimensions of the plates to minimize accumulated errors due to tolerancing.

The larger metal components, including the three plates, flap, frames, access panel and its backing plate, and the quarter-wheels, will be machined from 6061 aluminum using a CNC router table. The main aluminum pieces have a longitudinal tolerance of 0.188” and transverse of 0.375”, over a span of six feet. These indicate how much the plates can deviate from flatness over that length. The nose will be produced using fused deposition modeling

(FDM) in PETG at 75% infill, selected for its favorable combination of stiffness, thermal resistance, and surface quality for a large, non-load-bearing part. The infill will help the channels and cavities be as airtight as possible. Traverse inserts will be printed in PLA with 30% infill, as lower mechanical demands and faster printability make it a suitable choice to meet the fit tolerances needed.

As mentioned before, all fasteners on the plate surface will be countersinks and the depth of these will be controlled with a stopper to make them as flush as possible with the surface, before covering them with speed tape to achieve a smooth surface during testing.

4.5 Assembly and Installation

For design validation and use, the splitter plate will be brought into the KWT, where all large pieces will be lifted into the test section using a crane. To install the splitter plate, the first parts to be mounted on the wall will be the four frames with their corresponding wall-side brackets. These will be threaded into pre-drilled holes on the walls, positioned at the previously specified locations shown in Figure 4.11. To prevent these frames from sagging once mounted on the wall, a set of wooden blocks will be placed between the floor and the first frame, and consecutively between each pair of frames. These will then be removed as the frames are secured to the plates. Following this, the brackets corresponding to the plate-side will be bolted to the frames, and the corner 45°brackets will be bolted into the chamfers.

The body plates are then secured, one at a time, positioning them upright and parallel to the tunnel wall. Starting with all three plates laying on the ground, their front sides facing the ceiling. The pressure taps along all three plates will have been set before the plates are set on the test section. This involves setting the 5866-06 Scannivalve 90°pressure tap on each of the drilled holes. This step for the pressure taps will only need to be done the first time the splitter is being set up. The tubing will be inserted and connected during mounting to properly set up the pressure measurement system. As the plates are mounted onto the frames, these tubes will be gathered with zip ties and secured to the frames, guiding them out of the test section, through the tunnel wall. Along with the pressure taps setting, the

back frame of the access panel will also be mounted onto the center plate, while in the entry bay, before entering the test section.

To begin, the D-ring anchor will be threaded into the top of the plate, and the crane will lift it into position against the frames. The first set of C-channels will be mounted onto the plate, and then set in the cutout position by the streamwise frames. The plate will be aligned with the brackets and secured by threading in the bolts. Once this plate is in position and secured to the frames, the leading edge will be fastened on. The middle plate will then be prepared for installation and lifted into place by the crane. The remaining c-channel set will then be bolted onto the middle plate and set in place in the following cutout of the frames. The plate will be set into position and bolted to the frames and to the channels connecting it to the leading edge plate. At this stage, an inspection will be performed to ensure that the edges of the two plates are properly aligned and that the surface is smooth and continuous. If any misalignment is found, the middle plate will be brought down and the connecting channels will be shimmed as needed. The plate will then be reinstalled and the alignment rechecked. This process will be repeated until a satisfactory, well-aligned joint is achieved. Once these two are set up, the trailing edge plate will be prepared and lifted up into position, following the same process as the previous plates. Once in place, the flap will be fastened onto it. For this process, a set of hinges will connect the plate and the flap at the needed distance. Following, the angle adjusting wheels will be attached to the flap. The flap will also count with a D-ring anchor point that will be used as an anchor point. The same alignment validation and shimming process mentioned previously will then be followed between the trailing and middle plate.

Having finished this process, the splitter plate should be fully mounted on the test section, supported by the frames and corner angle brackets, with the three plates resting on the floor. As mentioned before, a gap of 3/8” will be left between the ceiling and the splitter, which will be covered with speed tape to seal it properly. This tape will also then be placed over the fasteners and seams between the plates. At this point, any additional feature will be mounted or set on the plate. This can include the pitot-traverse, the traverse inserts, the

access panel (which will also need to have the pressure tap Scannivalve piece and tubing fitted), and any tripping devices towards the leading edge.

4.6 Calculations supporting splitter plate design

With the design complete, the next step was to verify that the plate is stiff enough to maintain the gap beneath the test article and that the number and size of fasteners are sufficient to hold the structure together. All fastener and loads calculations must exceed the KWT's factor of safety of five. A load scenario was set to be a tunnel air speed of 90 m/s (200 mph) and a plate angle of 10°, which is considered a conservative worst-case. This angle was chosen solely to ensure that the result would be conservative, as the plate will not experience anything close to this angle in use. This extreme plate angle results then in a much higher load experienced towards the leading side of the plate. For this reason, the load distribution was assumed to be 70/30, where the first 30% of the plate's length (first body plate) will be experiencing 70% of the loads. Following thin airfoil theory, for a flat plate the lift is acting at the quarter chord distance and the lift coefficient, C_L, can be determined by Eq.4.4 [37].

$$C_L = 2\pi\alpha \tag{4.4}$$

$$L = C_L q A \tag{4.5}$$

where α is the AoA. Thus, assuming a 10°AoA on the plate and an airspeed of 90 m/s - corresponding to a dynamic pressure of 4 kPa (84 psf)- the total lift can be estimated to be 9,110 lbf. From these, an approximate pressure difference over the plate's area can be determined to be 5456 PA (0.791 psi).

4.6.1 Splitter plate and frame stiffness

To assess the stiffness of the plate and supporting frames, finite element analysis (FEA) was conducted in ANSYS using separate models for each component. For the plate, a simplified CAD model was used that included the three aluminum plates and integrated access panel, but excluded fasteners, brackets, and channels. Instead of explicitly modeling these hardware components, boundary conditions were applied at representative attachment points: fixed supports were placed at the plate corners to simulate the corner brackets, while remote displacement constraints were applied at bracket and channel locations to approximate load transfer to the supporting structure. A static structural analysis was performed using solid elements and 6061-T6 aluminum material properties. The applied load, corresponding to a total aerodynamic lift of 9,110 lbf, was modeled as a pressure distributed across the plate, with 70% concentrated on the first 30% of the chord in accordance with flat plate theory assumptions discussed previously. The mesh was generated with automatic sizing and refinement in areas of expected high deformation, producing an unstructured triangular volume mesh. A mesh sensitivity check was performed by locally refining elements near the leading edge, confirming convergence of the maximum displacement within acceptable tolerance. Under these conditions, the maximum deformation was found to be 1.42 mm (0.056”), as shown in Figure 4.12. Comparing these results to the previously estimated boundary layer stand-off height at the center (12.88 mm), the maximum deformation represents approximately 11% of the stand-off gap. These results indicate that even under worst-case loading scenarios, the plate deformation remains well within the requirement of less than 15% and will not come into contact with the base of any model mounted above it.

The same testing and load conditions were used for the frame FEA, assuming that the plate’s load is distributed evenly between all four frames. Once again, remote displacement and fixed supports were used to simulate the brackets on both the wall and plate sides. These obtained a maximum deformation of $5.91E-5$ inches, as shown in Figure 4.13. Meaning, the frames will remain dimensionally correct throughout testing.

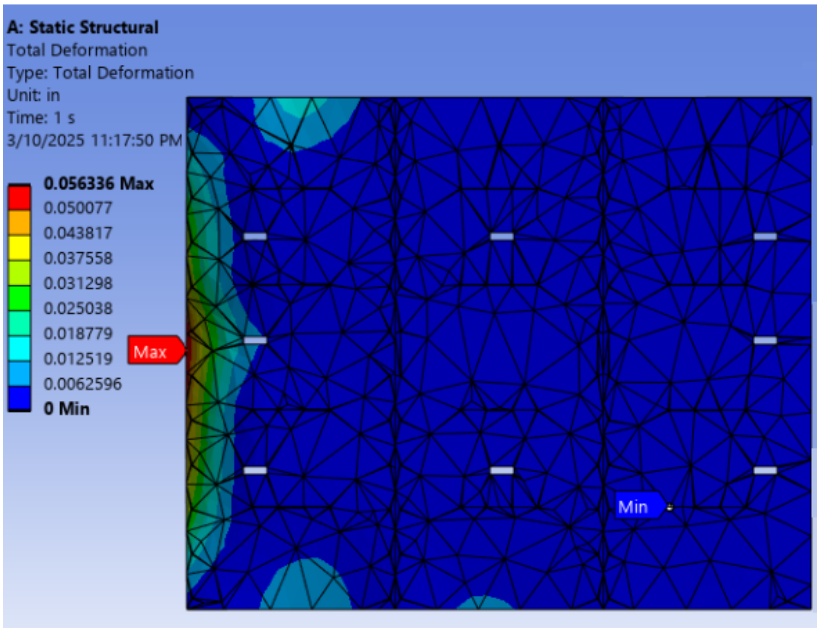

Figure 4.12: FEA Total Deformation Distribution - Plates

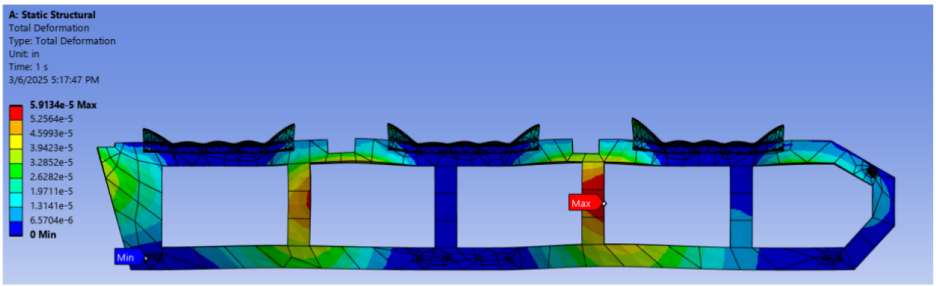

Figure 4.13: FEA Total Deformation Distribution - Frame

4.6.2 Fastener sizing

To analyze the load distribution over the fasteners, the same aerodynamic loading from the flat plate airfoil approximation was used, applying a total lift of 9,110 lbf with a 70/30 split between the leading and trailing sections of the plate. A detailed tension and shear analysis was then carried out for each fastener group, depending on their role in the structural assembly. Bolts connecting the plate to the brackets and the tunnel wall were assumed to carry tensile loads, while bolts connecting the angle brackets to the frames were assumed to carry shear loads, based on their relative orientations and force transfer paths. These assumptions are illustrated in Figure 4.14 with the bolts in tension marked with blue, and those in shear with orange.

The analysis followed standard bolt strength calculations as presented in the NASA Fastener Design Manual [38]. Tension capacity was determined using the tensile stress area of the bolt threads and the ultimate tensile strength of 316 stainless steel, taken as 70,000 psi. Shear capacity was approximated using 45% of the tensile strength to reflect the reduced strength under shear, consistent with conservative design practice. The formulas used were:

$$F_{\text{tension}} = A_t \cdot \sigma_{\text{tensile}} \quad \text{and} \quad F_{\text{shear}} = A_s \cdot \tau$$

where A_t is the tensile stress area, A_s is the shank cross-sectional area, σ_{tensile} is the ultimate tensile strength, and τ is the shear strength. Material moduli were not directly required for this strength-based analysis, as the goal was to compare load demand to allowable load based on ultimate strength and geometry.

To ensure a conservative result in line with the Kirsten Wind Tunnel's design standards, a safety factor (SF) of 5 was applied to all maximum capacity values by dividing the raw capacities accordingly. Table 4.2 summarizes the resulting allowable loads for each type of fastener, alongside the estimated expected load per bolt based on the distributed aerodynamic force and the quantity of fasteners used.

All of the expected loads are more than 50% below the maximum capacity that already

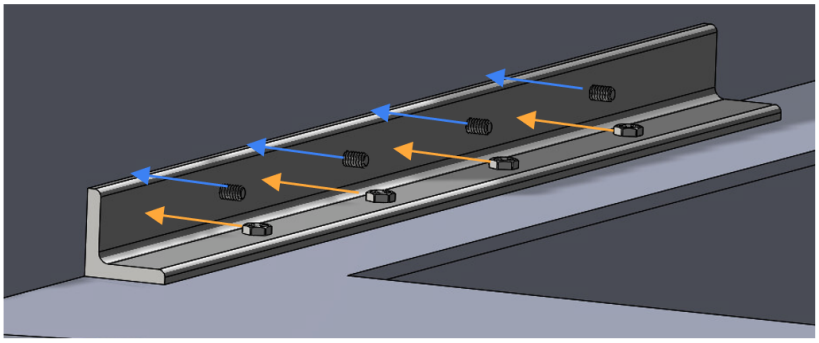

Figure 4.14: Bolts in tension and shear on the brackets.

Bolt Type	Location	Total Quantity of Bolts	Tension/Shear	Capacity w/ SF of 5	Expected load/fastener
1/4 - 20 (Leading Plate)	Plate to bracket	20	Tension	445 lbf	136.7 lbf
1/4 - 20 (Leading Plate)	Bracket to frame	20	Shear	245.5 lbf	136.7 lbf
1/4 - 20 (Downstream Plates)	Plate to bracket	32	Tension	445 lbf	199.3 lbf
1/4 - 20 (Downstream Plates)	Bracket to frame	32	Shear	245.5 lbf	199.3 lbf
3/8 -18	Tunnel to bracket	36	Tension	1,085 lbf	145 lbf
3/8 -18	Bracket to frame	36	Shear	971 lbf	16.1 lbf

Table 4.2: Fastener load distribution

Bolt Type	Bolt Material	Threaded Material	Thread engagement length	Force direction	Thread pull-out strength
1/4 - 20	Alloy Steel	Aluminum	1/4”	Tension	1,785 lbf
1/4 - 20	Alloy Steel	Aluminum	3/8”	Tension	2,678 lbf

Table 4.3: Fastener thread pull-out calculations

accounts for the safety factor of 5. As a result, the number and types of fasteners selected will be sufficient, even at the most extreme load scenarios.

Finally for the thread pull out calculation, two different fastener types were analyzed. First the 1/4-20 bolts that go in through the front of the plates and bolt to a piece on the back (brackets or channels). For this calculation the relevant aspects were the fastener type, the materials of the bolts and the threading pieces, the thread engagement length and the applied force direction; all of these and the found pull-out strength can be seen in Table 4.3 for all the required fasteners. The thread pull-out strength was estimated based on a simplified shear model along the engaged threads, following procedures described in the NASA Fastener Design Manual [38]. The governing equation used was:

$$F_{\text{pull-out}} = \pi \cdot d_{\text{minor}} \cdot L_e \cdot n \cdot \tau$$

where d_{minor} is the minor diameter of the internal thread, L_e is the thread engagement length, n is the number of threads per inch, and τ is the shear strength of the weaker material (typically the tapped component). This approach assumes shear failure along the cylindrical surface formed by the engaged threads.

The second type of fasteners to be analyzed for thread pull-out are those threaded directly into the tunnel walls. As mentioned previously, these are threaded onto different tunnel wall surfaces with approximately the same thread engagement length but varying between steel and aluminum for threaded material. The parameters and final pull-out strength for these can be seen in Table 4.4.

To incorporate the required safety factor, the calculated pull-out strength is divided by

Bolt Type	Bolt Material	Threaded Material	Thread engagement length	Force direction	Thread pull-out strength
3/8-16	Alloy Steel	Aluminum	1”	Tension	312,000 lbf
3/8-16	Alloy Steel	Steel	1”	Tension	561,000 lbf
3/8-16	Alloy Steel	Aluminum	1.75”	Tension	546,000 lbf
3/8-16	Alloy Steel	Steel	1.75”	Tension	982,000 lbf

Table 4.4: Fastener thread pull-out calculations

five and compared against the expected loads presented in Table 4.2. Since the reduced pull-out strength remains greater than the anticipated loads, it is confirmed that the fasteners will not fail due to thread pull-out.

Having gone through the previous validation calculations, it can be stated that the design prepared for this splitter plate complies with the required standard on all three items: stiffness, load distribution, and thread pull-out.

Chapter 5

TEST PLANS & INSTRUMENTATION

5.1 Test Plan Overview

The tests carried out will allow for the validation of the splitter plate system. They will confirm that it functions as intended, can be used in the tunnel without issue, and provide a baseline characterization of the flow around it for future model integration. The main goals of the tests will be to: (1) Verify the uniformity of the boundary layer and pressure across the splitter plate for a range of velocities, (2) verify the performance of the diffuser behind the splitter plate, (3) ensure flow uniformity in the test section with the presence of the splitter plate. The goal is to run these tests within a three-day span. Several measurements will be taken to meet these goals. A pitot-traverse inserted into the splitter plate at different locations will be used to characterize the boundary layer on its surface. Pressure scanning will capture the pressure distribution across the plate. Tufting on the diffuser, combined with illumination, will provide flow visualization to assess the splitter's influence in that region. Additionally, a pitot tube mounted on the tunnel's traverse will measure flow uniformity at the plane entering the test section. The velocities proposed for these tests are 10m/s, 35 m/s and 80 m/s, to obtain data for low, middle and high tunnel velocities.

The overall test sequence will proceed through the following steps:

1. Verify flatness and perform shim adjustments once the splitter plate is mounted in the tunnel.

2. Set and adjust the flap to locate the stagnation point.

3. Conduct diffuser flow visualization and return pressure diagnostics.

4. Measure inflow uniformity at the test section entrance.

5. Run pressure uniformity scans across the plate pressure taps.

6. Measure boundary layer profiles on the plate surface.

5.2 Verification of plate gaps and flatness

Before any flow measurements are conducted, the splitter plate assembly must be inspected to confirm that it meets the required geometric tolerances. This includes verifying the integrity of the assembly, ensuring the plates are properly seated with continuous contact along the test section wall, and checking for any unwanted gaps or misalignments that could introduce flow disturbances. Flatness is a critical factor in maintaining boundary layer quality across the plate. Deviations from the intended surface geometry can trip or distort the boundary layer, undermining the purpose of the splitter.

To evaluate this, a precision straight edge of 48 inches in length will be placed flush along the splitter plate at multiple horizontal and vertical positions. The length was selected to provide coverage over a representative portion of each panel without being unwieldy during installation. Gaps between the straight edge and the plate surface will be checked using feeler gauges ranging from 0.001 to 0.010 inches. Flatness is considered acceptable if no gap exceeds 0.008 inches across the measured span, corresponding to roughly 15% of the average standoff height of 0.51 inches. If discontinuities or steps are observed, shims will be inserted or other adjustments made to bring the surface back into specification. This process ensures continuity across the span of the splitter and proper alignment with the test section.

These inspections may be repeated after initial runs to verify that the plate has not shifted or deformed under aerodynamic loading. Once flatness and gap tolerances are confirmed, the plate can be considered ready for flow characterization and pressure measurements. If there are deviations from flatness or surface quality issues in the plate, these could compromise the validity of the boundary layer and measurements related to it. If any issues arise during the flatness evaluation, additional shimming can be done as necessary to correct small deflections.

Buffing or polishing of the splitter might be required if there are any excessively rough patches. If the deviations are greater than the set threshold, additional structural supports might be considered and added to the frame system. In a worst-case scenario where the plate material does not meet tolerances even after adjustments, a higher tolerance stock material should be obtained and any relevant pieces replaced or remade.

5.3 Setting the plate stagnation point using the flap

To ensure the splitter plate's leading edge is operating as intended and not introducing additional disturbances such as premature separation or asymmetry, the location of the stagnation point must be controlled. This is achieved by adjusting the trailing edge flap, which alters the pressure distribution and flow attachment along the plate. Even when the plate is positioned at zero geometric angle of attack, the stagnation point may not lie exactly at the geometric leading edge. Small geometric imperfections, flow non-uniformities, or pressure gradients along the tunnel can cause the stagnation point to shift above or below the intended location. If the stagnation point leans to one side, the pressure difference between both sides becomes asymmetric, with the side seeing slower flow experiencing higher pressure.

To identify and correct this, the pressure difference across the upper and lower cavities of the 3D-printed leading edge nose will be measured via static pressure taps. These taps are arranged symmetrically along the upper and lower surfaces of each leading edge section. The pressure differential serves as a proxy for the relative location of the stagnation point: the goal is to find the flap angle that produces near-zero pressure difference across the nose surfaces. This condition corresponds to symmetric stagnation, where neither side dominates the flow. Measurements will be taken using an MKS 226A21 Baratron differential capacitance manometer, which has a 20 Torr full-scale range and a resolution of 0.01% of full scale—equivalent to 2.7 Pa. Its analog accuracy is $\pm 0.5\%$ of full scale, providing reliable differential readings for the small pressure variations expected at the stagnation point. Signal acquisition is handled using a National Instruments PCIe 6361 16-bit data acquisition

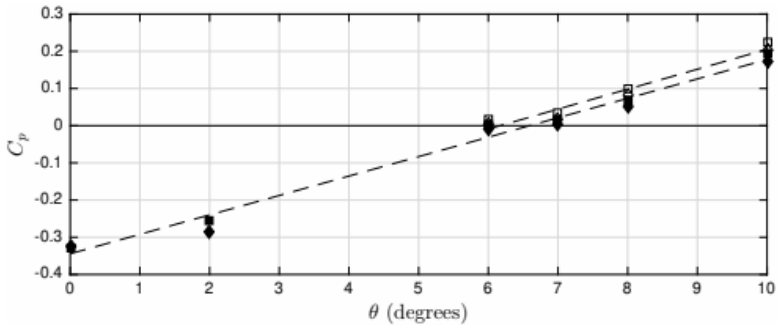

Figure 5.1: Pressure difference between upper and lower surface static pressure from Boeing Bump tests [8].

system, which ensures digital resolution finer than the sensor's analog limit.

Flap positions are set mechanically using pairs of locating bolts, as described in an earlier section and shown in Figure 4.8. Tests will begin with the flap at 0°, and will proceed through a range of positive and negative angles based on observed pressure trends. For each angle, the differential pressure across each tap pair will be recorded. The angle that minimizes the pressure difference—ideally driving it to zero—will be designated the stagnation-centered configuration. The process will first be conducted using the centerline tap pair. Once the optimal angle is identified, pressure differences across all other spanwise tap pairs will be evaluated to confirm that the stagnation point lies uniformly along the leading edge. If strong spanwise variation is detected, further adjustment may be necessary. This approach mirrors that used by Williams et al. [8] for the Boeing Bump splitter plate in the 3x3 tunnel. As shown in Figure 5.1, the optimal flap angle in their case was found at 6°, corresponding to a zero pressure difference ($C_p \approx 0$) across the nose. A similar trend is expected here.

This procedure will be repeated at multiple test velocities to ensure consistency and should be repeated during actual model testing to confirm that the stagnation location remains stable under relevant flow conditions.

5.4 Stall of the Diffuser

Part of validating the performance of the wind tunnel's circuit with the splitter plate, will be to assess whether the diffuser is experiencing stall. Being a continuous wind tunnel, the KWT relies on the diffuser to recover pressure and reduce flow velocity downstream of the test section. This improves the tunnel efficiency and allows operations to run smoothly and with low turbulence. Since the diffuser functions with an adverse pressure gradient, it is susceptible to flow separation, especially if there is some disturbance or blockage upstream increasing back-pressure, which could be the case with the splitter. Setting up the splitter plate in the test section not only creates blockage for the flow, but can also have an effect on the flow path and wall boundary layer upstream of the diffuser. This can result in increased turbulence or asymmetries that can trigger separation or stall on the diffuser walls. This would lead to a significant loss in the pressure recovery process, affecting the return overall and likely uniformity at the inlet; or to backflow effects moving towards the upstream section.

To obtain diagnostics on this area, tufts will be placed on the surfaces of the diffuser to act as local flow direction indicators. If the flow is attached, the tufts will be aligned smoothly with the expected local velocity vector, while in separated flow they will oscillate, point elsewhere (i.e., upstream), or flap around with no order. To enhance visibility, the diffuser will be illuminated using high-intensity LED panels placed externally and angled to avoid glare while providing uniform lighting across the tuft field, or with LED strips placed on the test section surfaces. Figure 5.2 shows the setup for this test in the KWT, with the tufts placed along the wall and floor, and the lighting strip beneath one of these rows of tufts.

This lighting setup ensures that even subtle tuft motion is clearly visible in recordings, particularly during low-speed or marginal stall conditions. The test will be carried out at various tunnel speeds to identify the presence and onset of stall, as well as to map the spatial extent of any separated regions. The entire testing process will be video recorded to allow detailed post-test review and analysis. If stall is observed during flow visualization, a solution

(a) View of the diffuser, facing downstream.

(b) View of the tunnel side wall.

Figure 5.2: Diffuser flow visualization with tufts at the KWT.

for this might be to install vortex generators near the diffuser entrance. These elements are meant to energize the boundary layer and delay separation. This test can be carried out simultaneously to any of the other tests.

5.5 Test Section Inflow Uniformity with Splitter Plate

Following the previous section and its focus on the effect of the splitter upon the wind tunnel's flow, inflow uniformity will be studied as well. As mentioned previously, setting up the splitter plate in the test section has the potential to alter the inflow uniformity at the entrance. It may introduce asymmetries, local flow acceleration, or pressure gradients into the otherwise uniform free flow. These can arise from misalignments, non-smooth surfaces, interference of the overall structure, or wake effects after the plate. While diffuser stall is a possible cause of non-uniform inflow, asymmetries can also develop in the absence of stall due to uneven pressure recovery between the two return legs of the tunnel. This effect can become more pronounced when the splitter is installed, especially if it shifts the balance of flow between the upper and lower circuits. For this reason, it is critical to verify that the inflow remains uniform while the splitter plate is in use.

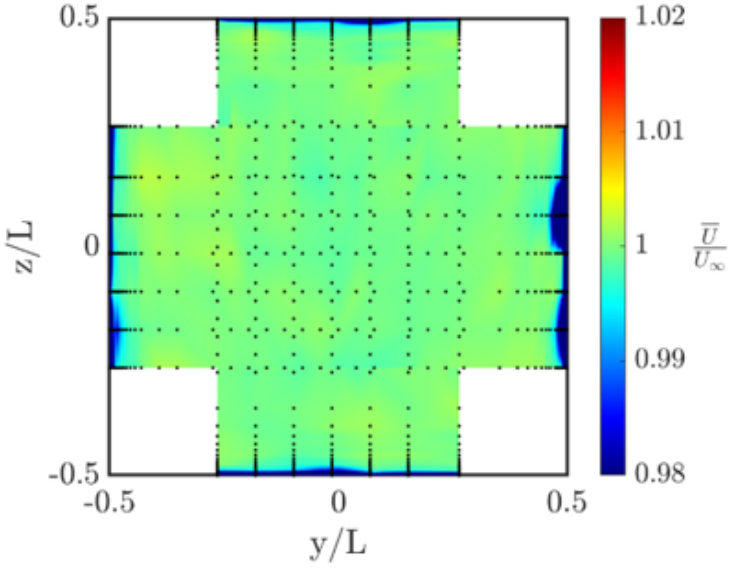

Figure 5.3: Mean uniformity data obtained at the 3x3 Wind Tunnel [9].

These measurements will be taken using the KWT's traverse system mentioned previously. This enables the positioning of a pitot tube probe throughout the inlet of the test section; moving horizontally across the centerline. The traverse system can move the pitot tube with a precision of 0.1" in all three dimensions [34] and its motion can be programmed for the sweep needed. This pitot would be connected to a pressure transducer. The data acquisition system for these measurements will be the KWT's standard DAQ consisting of a dual-processor 150-MHz Pentium Pro PC with a 16-bit analog to digital converter -National Instruments PXIe chassis system. Data will be acquired and averaged at a sampling rate of 100 samples per second, and each test point consists of five seconds of on-condition data [5].

The results will show the mean inflow uniformity, as the example shown in Figure 5.3, from data obtained at the three-by-three wind tunnel at the University of Washington [9]. These will be comparable to the baseline measured flow conditions without the splitter.

5.6 Measurement of pressure uniformity

To assess the aerodynamic quality of the splitter plate and verify that it does not introduce significant pressure gradients, surface pressure taps distributed across the plate will be sampled at a range of tunnel velocities. These measurements allow for the evaluation of streamwise and spanwise pressure gradients, which influence boundary layer development and may indicate zones of acceleration or deceleration.

All 32 taps on the splitter surface—distributed as shown in Figure 4.4—are connected to a Scanivalve circular selector (Figure 5.4) with 48 ports, enabling sequential sampling through a single pressure transducer. Tap 1, located near the leading edge on the centerline and marked in Figure 4.4, serves as the reference pressure. The pressure data are acquired using a 20 Torr MKS Baratron pressure transducer and a 16-bit NI PCIe-6361 data acquisition system, as described in the stagnation point section. The differential signals between each tap and the reference are logged to compute pressure coefficients and spatial pressure gradients. The resolution of the pressure measurement system—approximately 0.267 Pa from the transducer (0.01% of full scale) and 0.81 Pa from the digital resolution—yields a combined effective resolution better than 1 Pa. This performance permits the detection of small yet meaningful streamwise pressure gradients across the splitter plate.

Rather than using the Clauser pressure-gradient parameter β, the acceleration parameter K is employed as a criterion for evaluating flow acceleration effects on boundary layer development, and determining if the boundary layer is canonical or not. A reference threshold of $K = 1.6 \times 10^{-6}$[27], considered to represent negligible acceleration influence and zero pressure gradient, is used to determine whether the measurement system can resolve relevant gradients to determine this.

To evaluate this, the formulation for K from Eq. 2.11 is used. The kinematic viscocity is estimated from standard atmospheric conditions at room temperature. The streamwise velocity gradient is approximated from static pressure tap measurements along the splitter, using Bernoulli's equation to relate pressure to velocity. For the tap spacing of 0.435 m (based

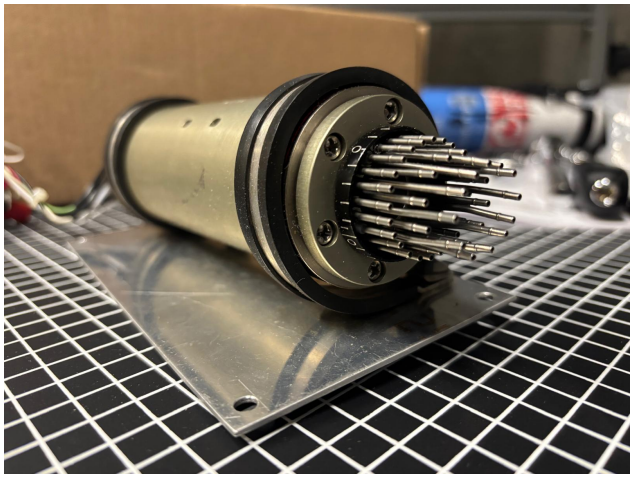

Figure 5.4: Scanivalve Circular Selector

on 8 taps over a 120 inch plate), the minimum resolvable pressure differences corresponding to $K = 1.6 \times 10^{-6}$ were calculated for three tunnel velocities. At 10 m/s, the required ΔP is approximately 5.6 Pa; at 35 m/s, it increases to 238 Pa; and at 80 m/s, it reaches approximately 1775 Pa. All of these pressure changes are well within the resolution capacity of the measurement system, especially at moderate and high speeds where the signal-to-noise ratio is larger. Even at the lowest velocity, the system is capable of resolving the gradient with acceptable confidence.

These results confirm that the system is well-suited for verifying that the flow over the splitter plate exhibits minimal acceleration and satisfies the near-zero-pressure-gradient condition required for canonical turbulent boundary layer development.

One important factor in obtaining reliable surface pressure measurements is the Reynolds number based on the tap diameter. The splitter's $\frac{1}{32}$" (0.7938 mm) diameter pressure taps yield the following Reynolds numbers based on the planned test velocities: $529 < Re_d < 4233$. According to Wuest [39], these values fall within a suitable range for accurate pressure transmission. Below $Re_d \approx 500$, viscous effects may dominate inside the tap, delaying or damping pressure signals. Above $Re_d \approx 5000$, flow may intrude into the tap, producing

artificially elevated readings. The current Reynolds number range avoids both extremes, meaning the taps are expected to operate without viscous lag or measurement bias due to flow intrusion.

5.7 Boundary Layer on the Splitter Plate

The boundary layer on the splitter plate will be measured using a pitot tube mounted on a precision traverse system. This traverse enables fine control of the probe position normal to the surface, allowing resolution of the steep velocity gradients near the wall that characterize turbulent boundary layers. The traverse is inserted from the backside of the splitter and indexed at predefined positions to establish a repeatable initial offset from the wall, denoted as z_0. This calibrated origin is critical for reliable near-wall alignment and accurate measurement of velocity profiles.

An example of the boundary layer data expected from this test is shown in Figure 5.6, which presents experimental and simulated profiles obtained using the same pitot-traverse system for the Boeing Bump project [10]. These measurements were taken at the same streamwise location across three velocities. The rightward shift of the wake region with increasing speed is consistent with higher Reynolds number development and serves as a baseline for the type of results targeted in the current work.

The traverse system was originally designed and validated by Williams et al. [10] and features a Velmex UniSlide stage driven by a LIN Engineering 417 stepper motor; as seen in Figure 5.5. Position feedback is provided by a Heidenhain LS477 encoder with 1 μm resolution, ensuring precise control and knowledge of probe location during measurements. This encoder resolution corresponds to a wall-unit step size $\Delta z^+ \approx 0.03$ at typical test conditions, enabling highly precise profiling within the viscous sublayer and logarithmic regions of the boundary layer. The pitot tube has an outer diameter of 0.02" (0.508 mm), and the closest physically resolvable distance to the wall is approximately half this diameter, or around 0.254mm. This minimum z_0 is verified using a macro-photography method that captures the pitot tip and its mirror reflection on the traverse base, calibrated by the known

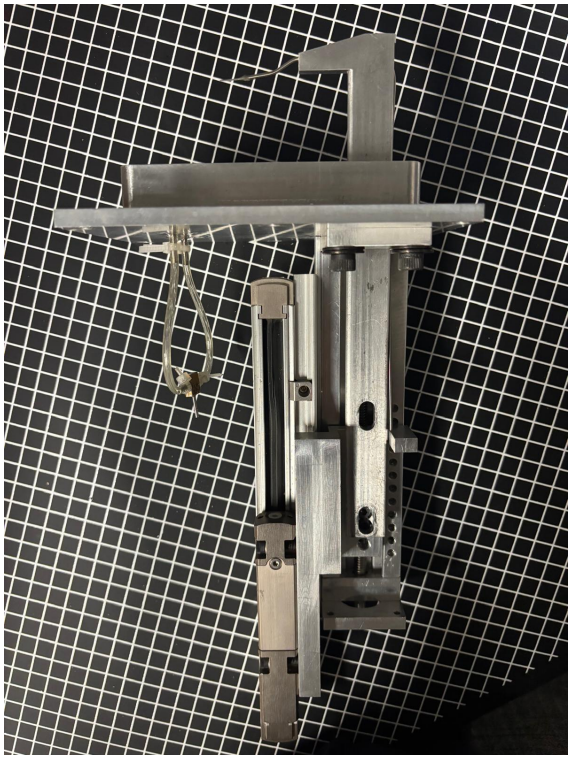

Figure 5.5: Pitot-Traverse Built for the Boeing Bump Project.

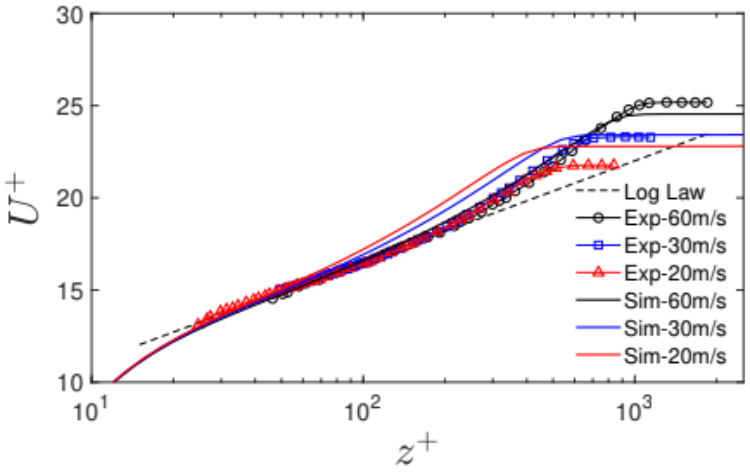

Figure 5.6: Example of Boundary Layer Profile Data Obtained with the Pitot-Traverse [10].

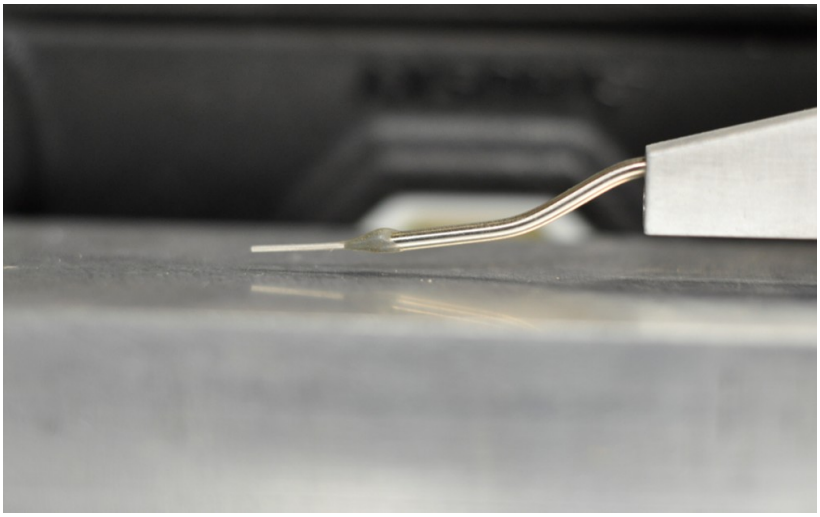

Figure 5.7: Macro photo of the pitot tube tip and reflection.

pitot diameter -such a photograph is shown in Figure 5.7. This technique, employed by Williams et al. [10], reduces uncertainty in the wall-normal offset and ensures that z_0 is accurately known, which is critical for subsequent velocity gradient and wall shear stress calculations.

To estimate the friction velocity u_τ, the skin friction coefficient C_f is first calculated using the empirical flat-plate turbulent boundary layer correlation for Reynolds number $Re_x = 1.03 \times 10^7$ -corresponding to the location where the model would be mounted in the splitter plate for average reference-, where

$$C_f = \frac{\tau_w}{\frac{1}{2}\rho U_e^2}[40].$$

From this, the wall shear stress is

$$\tau_w = \frac{1}{2}\rho U_e^2 C_f,$$

and the friction velocity follows as

$$u_\tau = \sqrt{\frac{\tau_w}{\rho}} = U_e \sqrt{\frac{C_f}{2}}.$$

Using this approach, u_τ is estimated for each freestream velocity U_e, allowing the calculation of the dimensionless wall distance

$$z^+ = \frac{z u_\tau}{\nu},$$

where z is the physical distance from the wall. The velocity in wall units, u^+, is obtained by normalizing the local velocity u as

$$u^+ = \frac{u}{u_\tau}.$$

Given the minimum resolvable physical distance $z_0 \approx 0.254\,\text{mm}$, and typical kinematic viscosity $\nu \approx 1.5 \times 10^{-5}\,\text{m}^2/\text{s}$, the estimated z^+ values at various freestream velocities are:

- **At 10 m/s:**

$$u_\tau \approx 0.36\,\text{m/s}, \quad z_0^+ = \frac{0.000254 \times 0.36}{1.5 \times 10^{-5}} \approx 6.1,$$

- **At 80 m/s:**

$$u_\tau \approx 1.15\,\text{m/s}, \quad z_0^+ = \frac{0.000254 \times 1.15}{1.5 \times 10^{-5}} \approx 19.5.$$

These values indicate that the pitot-traverse system can measure velocity profiles down to $z^+ \approx 6$ at low speeds and $z^+ \approx 20$ at higher speeds, sufficiently close to the wall to resolve the logarithmic region of the boundary layer, given the log region that is to be determined requires a resolution of $z^+ \approx 100$. The traverse's positional accuracy of 1 μm enables a fine spatial resolution on the order of $\Delta z^+ \approx 0.03$, which supports detailed characterization of near-wall velocity gradients. Velocity resolution is limited by the pressure measurement sensitivity, but the system is estimated to achieve velocity accuracy of approximately $\Delta u^+ \approx 0.02$, enabling identification of the velocity profile shape and wall shear stress.

The values of u_τ presented above are estimated using an empirical correlation for C_f, and are only intended to provide approximate values for computing z_0^+. These estimates are useful at the planning stage to evaluate whether the measurement system has sufficient spatial resolution to capture the near-wall behavior. However, they are not used for determining the final value of u_τ from the actual boundary layer data. For the final datasets, u_τ will not be obtained through empirical methods due to their inherent uncertainty. Instead, the approach will rely on fitting the measured velocity profile in inner coordinates to the expected log-law behavior. A value of u_τ is selected and used to normalize the mean velocity data into wall units u^+ and wall-normal coordinate y^+. The resulting profile is then compared to the canonical logarithmic law:

$$u^+ = \frac{1}{\kappa} \ln y^+ + C,$$

where $\kappa = 0.41$ and $C = 5.2$ are the chosen constants. The estimate of u_τ is adjusted until a region of the profile collapses onto this log line. A valid log region is expected to fall within $30 < y^+ < 0.1\delta^+$, where $\delta^+ = \delta u_\tau / \nu$. If the log region aligns with this range and shows consistent overlap, the selected u_τ is considered a reliable representation of the friction velocity. This process allows for a more robust, data-driven determination of u_τ that reflects the actual flow behavior over the splitter plate.

In summary, by combining the empirical skin friction coefficient correlation with precise traverse positioning and pitot velocity measurements, the system is capable of generating high-fidelity boundary layer profiles on the splitter plate. This facilitates accurate extraction of u_τ, z^+, and u^+, critical for validating simulations and understanding the flow physics in this test.

Chapter 6

CONCLUSION

This work has outlined the full design and validation strategy for a splitter plate intended to generate a canonical, zero-pressure-gradient turbulent boundary layer for half-span model testing in the Kirsten Wind Tunnel. The splitter plate was required to meet a stringent set of quantitative and qualitative criteria: (1) fit precisely within the KWT test section while avoiding the 45° chamfers, requiring an 8-by-10 ft profile set 18" off the wall; (2) ensure a flatness tolerance within 15% of the model stand-off distance (estimated baseline of 12.88 mm); (3) enable repeatable boundary layer development via a smooth rounded leading edge and minimal pressure gradients; (4) allow for modular, repeatable installation with sufficient access to all mechanical and diagnostic components; and (5) comply with the facility's safety factor of five. Empirical estimates predicted boundary layer thicknesses of 25–40 mm and displacement thicknesses of 3–5 mm along the length of the model, informing both the stand-off gap -targeted initially at $4\delta^*$- and flatness criteria.

Ensuring the splitter plate met aerodynamic and structural performance targets required addressing several nontrivial fabrication challenges. Flatness was the most critical, particularly with potential interference from fasteners or joints on the surface. Given the size of the aluminum plates used (39 by 95.625 inches) and the router's fabrication tolerance of 0.030 inches, additional steps were necessary to maintain the required surface quality. To counter these limitations, C-channel reinforcements and selective shimming were applied to promote flatness. Components requiring tighter tolerances were manufactured after the initial cuts, using the actual plate dimensions and smaller equipment capable of higher precision. Blockage effects were also carefully managed to avoid disrupting the flow in the test section or downstream diffuser. The frame was aligned with the flow direction and included cutouts

to reduce resistance, while all fasteners were countersunk and covered with aluminum tape to smooth the surface. These strategies collectively minimized flow disturbances due to surface defects or misalignments. The final design fulfills its primary objective: to provide a well-characterized, repeatable inflow with minimal disturbance. The boundary layer is expected to remain turbulent, spanwise uniform, and under near zero pressure gradient conditions. Embedded instrumentation—including 32 static pressure taps and 9 boundary layer probe locations—enables detailed flow monitoring and ensures repeatability and stagnation point control across the test envelope. At present, the splitter plate is under fabrication. Router-cut structural components and 3D-printed leading edge elements are in progress. Once complete, brackets and inserts will be custom-drilled based on true hole locations, followed by modular assembly and installation into the KWT. The modular design ensures both repeatability and quick disassembly for diagnostics and potential iteration.

Validation testing is structured in phases. Initial steps involve mechanical inspection and flatness verification, followed by aerodynamic testing across a representative range of tunnel speeds, up to 90 meters per second. These tests will use surface pressure measurements, pitot traverse scans, and diffuser flow visualization. The goals of the campaign are to: (1) confirm the development of a canonical boundary layer, with an acceleration parameter $K < 5 \times 10^{-6}$; (2) verify the presence of a clear log law region and appropriate wake strength (Π approaching a constant); (3) demonstrate inflow uniformity across the section; and (4) assess whether the diffuser flow remains attached and stable under the influence of the splitter. Boundary layer profiles will be captured at several spanwise and streamwise positions, and compared directly to empirical growth laws. Pressure taps on the plate allow both spanwise and streamwise gradients to be detected, ensuring that no external pressure gradients are present and enabling real-time flap adjustments. Tunnel diagnostics, including total pressure surveys at the test section inlet and return leg, will confirm that the splitter does not introduce adverse effects across the facility. Preliminary resolution and tolerance studies confirm that the selected instrumentation and measurement techniques offer sufficient accuracy to resolve relevant flow features, including wall-normal gradients and pressure distributions. Together,

these elements ensure that the test campaign is capable of reliably determining whether the design goals have been met.

Once validated, the splitter will serve as a standardized symmetry plane for CRM-HL half-span model integration. The plate allows for an adjustable stand-off gap, for which a gap sensitivity study will need to be conducted. It also offers a robust base for mounting a variety of high-lift configurations and measurement systems, all without requiring complex sealing systems such as metric peniches or turntables. This marks a significant step forward in the tunnel's half-model testing capabilities. Ultimately, this splitter plate expands the experimental fidelity of the CRM-HL campaign. By providing stable, two-dimensional inflow conditions, it enables more direct comparisons with CFD predictions and improves the reliability of aerodynamic data acquired in the Kirsten Wind Tunnel. The result is a better-aligned synergy between experimental and computational research, supporting the broader objectives of the CFD 2030 vision.

REFERENCES

[1] Rivers, N. M., "HL-CRM," `https://commonresearchmodel.larc.nasa.gov/high-lift-crm/`, 2022, Accessed: 2025-06.

[2] S.B.A. Invent, "Boundary Layer," `https://sbainvent.com/fluid-mechanics/boundary-layer/`, Accessed: 2025-05.

[3] Zagarola, M. and Smits, A., "Mean-flow scaling of turbulent pipe flow," *Journal of Fluid Mechanics*, Vol. 373, 1998, pp. 33–79.

[4] Lin, J., Melton, L., Viken, S., Andino, M., Koklu, M., Hannon, J., and Vatsa, V., "High Lift Common Research Model for Wind Tunnel Testing: An Active Flow Control Perspective," *55th AIAA Aerospace Sciences Meeting - SCITECH*, Vol. 55, 2017, pp. 1–15.

[5] University of Washington, Aeronautics & Astronautics, "Kirsten Wind Tunnel (KWT)," `https://www.aa.washington.edu/AERL/KWT`, 2025, Accessed: 20125-04-06.

[6] Ho, K., Soltani, M., and Bragg, M., "Impact of Simulated Ice Shapes on a Wing," Tech. Rep. 2019-pd-pa-292, University of Washington, Seattle, WA, 2019.

[7] Shindo, S. and Rae, W., "Improvement of Flow Quality at the University of Washington Subsonic Wind Tunnel," *Journal of Aircraft*, Vol. 16, No. 7, 1979, pp. 419–420.

[8] Williams, O., Slotnick, J., Spalart, P., Ferrante, A., Samuell, M., Robbins, M., Sarwas, S., and Annamalai, H., "Development and experimental study of gaussian speed-bumo CFD validation test case for turbulent separated flows," Tech. rep., University of Washington and Boeing, Seattle, WA, 2020.

[9] Robbins, M., Samuell, M., Annamalai, H., and Williams, O., "Overview of validation completeness for gaussian speed-bump separated flow experiments," *Proc. of the AIAA SciTech 2021*, SciTech, AIAA, 2021.

[10] Williams, O., Samuell, M., Sarwas, S., Robbins, M., and Ferrante, A., "Experimental study of a CFD validation test case for turbulent separated flows," *AIAA SciTech 2020 Forum*, AIAA SciTech Forum, AIAA, Orlando, FL, 2020.

[11] Slotnick, J., Khodadoust, A., Alonso, J., Darmofal, D., Gropp, W., Lurie, E., and Mavriplis, D., "CFD Vision 2030 Study: A Path to Revolutionary Computational Aerosciences," Tech. Rep. CR-2014-218178, NASA Langley Research Center, Hampton, VA, March 2014.

[12] Evans, A., Lacy, D., Smith, I., and Rivers, M., "Test Summary of the NASA Semi-Span High-Lift Common Research Model at the QinetiQ 5-Metre Low-Speed Wind Tunnel," *Proc. of AIAA Aviation Forum*, AIAA Aviation, AIAA, Virtual Event, 2020, pp. 1–24.

[13] Skinner, S. and Zare-Behtash, H., "Semi-span wind tunnel testing without conventional peniche," *Exp Fluids*, Vol. 58, No. 163, 2017, pp. 1–18.

[14] Oberkampf, W. and Smith, B., "Assessment Criteria for Computational Fluid Dynamics Validation Benchmark Experiments," *Proceedings of the Aerospace Sciences Meeting*, Vol. 52, 2014, pp. 1–27.

[15] Hazen, D., "Film Notes for Boundary Layer Control," Tech. Rep. No. 21614, Massachusetts Institute of Technology, Cambridge, MA, 1968.

[16] Eder, S., Hufnagel, K., and Tropea, C., "Semi-Span Testing in Wind Tunnels," *Proc. of the 25th International Congress of the Aeronautical Sciences*, ICAS, ICAS, 2006, pp. 1–9.

[17] NASA Glenn Research Center, "Boundary Layer," `https://www.grc.nasa.gov/www/k-12/BGP/boundlay.html`, 2021, Accessed: 2024-May.

[18] Pope, S. B., *Turbulent Flows*, Cambridge University Press, 2000.

[19] NASA, "Boundary Layer," `https://www.grc.nasa.gov/WWW/BGH/boundlay.html`, 2021, Accessed: 2024-June.

[20] Coles, D., "The Turbulent Boundary Layer in a Compressible Fluid," Tech. Rep. R-403-PR, The Rand Corporation, Santa Monica, CA, Sept. 1962.

[21] Leishman, J. G., *Introduction to Aerospace Flight Vehicles*, Embry Riddle Aeronautical University, FL, USA, 2022.

[22] Chauhan, K., Monkewitz, P., and Nagib, H., "Criteria for assessing experiments in zero pressure gradient boundary layers," *Fluids Dynamics Research*, Vol. 41, No. 2, 2009.

[23] Balkumar, P. and Iyer, P., "Laminar to Turbulence Transition in Boundary Layers due to Tripping Devices," *Proc. of the 2021 AIAA Fluid Dynamics Conference*, AIAA Fluid Dynamics Conference, AIAA, Nashville, Tennessee, 2021, pp. 1–17.

[24] Lee, J. and Sung, H., "Effects of Adverse Pressure Gradient on a Turbulent Boundary Layer," *Proc. of the TSFP Conference 2007*, TSFP, TSFP, Munich, Germany, 2007, pp. 29–34.

[25]

[26] DeGraaff, D. and Eaton, J., "Reynolds-number scaling of the flat-plate turbulent boundary layer," *Journal of Fluid Mechanics*, Vol. 422, 2000, pp. 319–346.

[27] Patel, V., "Calibration of the Preston tube and limitations on its use in pressure gradients." *Journal of Fluid Mechanics*, Vol. 23, 1965, pp. 185–205.

[28] "Copyright," *Aerodynamics for Engineering Students (Seventh Edition)*, edited by E. Houghton, P. Carpenter, S. H. Collicott, and D. T. Valentine, Butterworth-Heinemann, seventh edition ed., 2017, p. iv.

[29] Schuster, D., "Aerodynamic Measurements on a Large Splitter Plate for the NASA Langley Transonic Dynamics Tunnel," Tech. Rep. TM-2001-210828, NASA Langley Research Center, Hampton, VA, March 2001.

[30] Doerffer, P. and Szulc, O., "High-Lift Behaviour of Half-Models at Flight Reynolds Numbers," *Task Quarterly*, Vol. 10, No. 01, 2006, pp. 191–206.

[31] Gatlin, G. and McGhee, R., "Study of Semi-Span Model Testing Techniques," *Proc. of the 14th Applied Aerodynamics Conference*, AIAA, AIAA, New Orleans, LA, 1996, pp. 1–20.

[32] Mamou, M. and Broughton, C., "CFD Investigation of the Aerodynamic Support Interference of a Semi-Span Model Equipped with a T-tail," Tech. Rep. STO-MP-AVT-338, National Research Council Canada, Montreal, Canada, 2021.

[33] Pulimeno, M., Schuster, D. M., Tu, E., Humphreys, B., Buggeln, R., Towne, A., and Jones, A., "Exploration of Stall Dynamics on a High-Speed CRM Wing Using Dynamic Mode Decomposition," *AIAA SciTech Forum*, January 2025, AIAA-2025-0876.

[34] Knowlen, C. and Hudgins, M., "Kirsten Wind Tunnel Flow Quality Assessment: 2018," *AIAA SciTech 2019 Forum*, AIAA SciTech Forum, AIAA, San Diego, CA, 2019.

[35] Stevens, H., "Wind Tunnel Boundary Layer Survey," .

[36] Cengel and Cimbala, "The Turbulent Flap Plate Boundary Layer," `www.me.psu.edu/cimbala/me320web_Spring_2015/pdf/Flat_plate_turbulent_BL.pdf`, 2015, Accessed: 2025.

[37] III, J. F. M., *Additional Aerodynamics Tools*, University Libraries at Virginia Tech, Blacksburg, VA, 2021.

[38] Barrett, R., "Fastener Design Manual," Tech. Rep. NASA-TP-10233, NASA Lewis Research Center, Cleveland, OH, 1990, Accessed: 2025-06-26.

[39] Wuest, W., "AGARD Flight Test Instrumentation Series Volume 11 on Pressure and Flow Measurement," Tech. Rep. AD A 090961, Advisory Group for Aerospace Research and Development, London, UK, July 1980.

[40] Smits, A., "Viscous Flows and Turbulence," Princeton University Department of Mechanical Engineering, Sept. 2007.

Appendix A

SPLITTER MOUNTING LOCATIONS ON THE TUNNEL WALL

This appendix provides the full list of splitter plate mounting coordinates used in the Kirsten Wind Tunnel. The mounting points are defined in inches with respect to the test section coordinate system, where the origin is located at the center of the test section. These locations correspond to where the brackets anchor the splitter plate structure to the wind tunnel wall. Positions are reported in radial coordinates (X, Y), where X is the horizontal axis (spanwise along the wall), and Y is the vertical axis (from the tunnel floor upwards).

The table below reorganizes the mounting points by increasing X position to facilitate visualization of their distribution across the wall span.

Mount Location	**Mount Location**	**Mount Location**
1 (-59.38, 12.63)	13 (49.84, -11.12)	25 (8.50, -11.12)
2 (-57.38, 12.63)	14 (47.84, -11.12)	26 (4.50, -11.12)
3 (-57.38, 28.56)	15 (49.84, -29.12)	27 (8.50, -29.12)
4 (-7.50, 12.63)	16 (47.84, -29.12)	28 (4.50, -29.12)
5 (-3.50, 12.63)	17 (-57.38, -29.12)	29 (0.48, -11.12)
6 (0.48, 12.63)	18 (-57.38, -11.12)	30 (0.48, -29.12)
7 (4.50, 12.63)	19 (-59.38, -11.12)	31 (-3.50, -29.12)
8 (8.50, 12.63)	20 (-7.50, 28.56)	32 (-7.50, -29.12)
9 (47.84, 28.56)	21 (-3.50, 28.56)	33 (-3.50, -11.12)
10 (49.84, 28.56)	22 (0.48, 28.56)	34 (-7.50, -11.12)
11 (47.84, 12.63)	23 (4.50, 28.56)	35 (-59.37, -29.12)
12 (49.84, 12.63)	24 (8.50, 28.56)	36 (-59.37, 28.56)

Appendix B

SPLITTER PLATE DRAWINGS

This appendix includes reference views of the custom splitter plate system designed for the Kirsten Wind Tunnel. The images document each component of the structure, including access panels, the supporting frame, segmented plates, and wheel supports. Views are provided to aid in interpretation of the mechanical design, spatial configuration, and mounting logistics. Images are grouped by component and presented in orthographic projection.

Access Panel

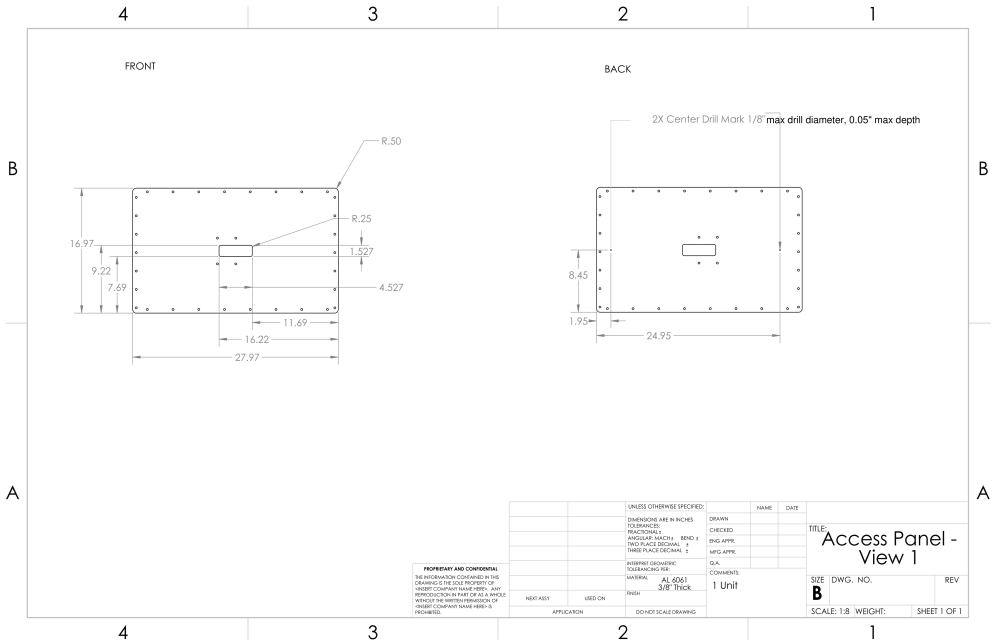

Figure B.1: Access Panel - View 1

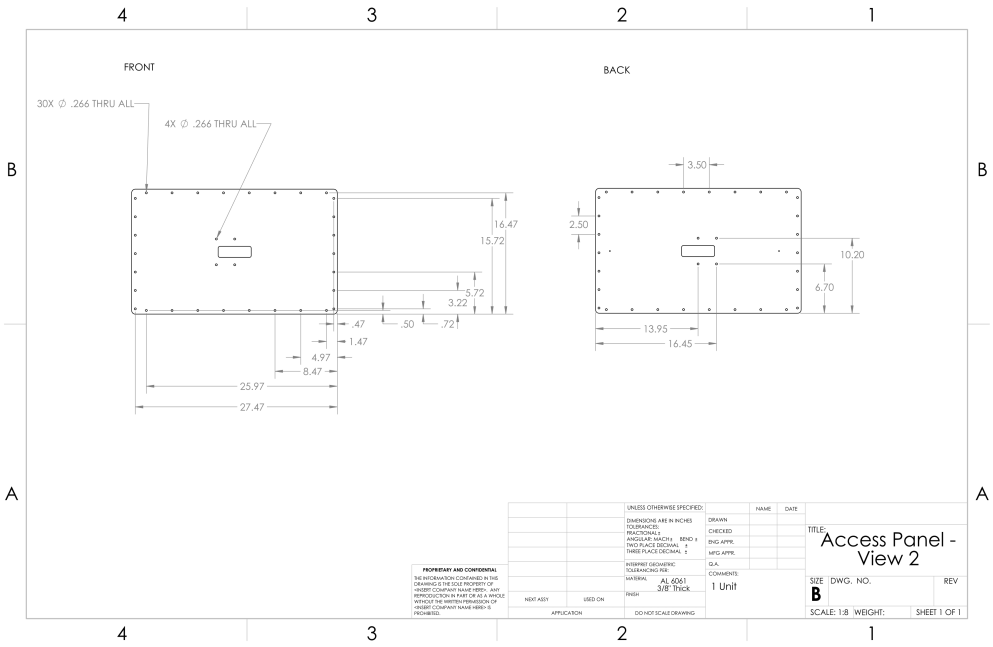

Figure B.2: Access Panel - View 2

Access Panel (Back Views)

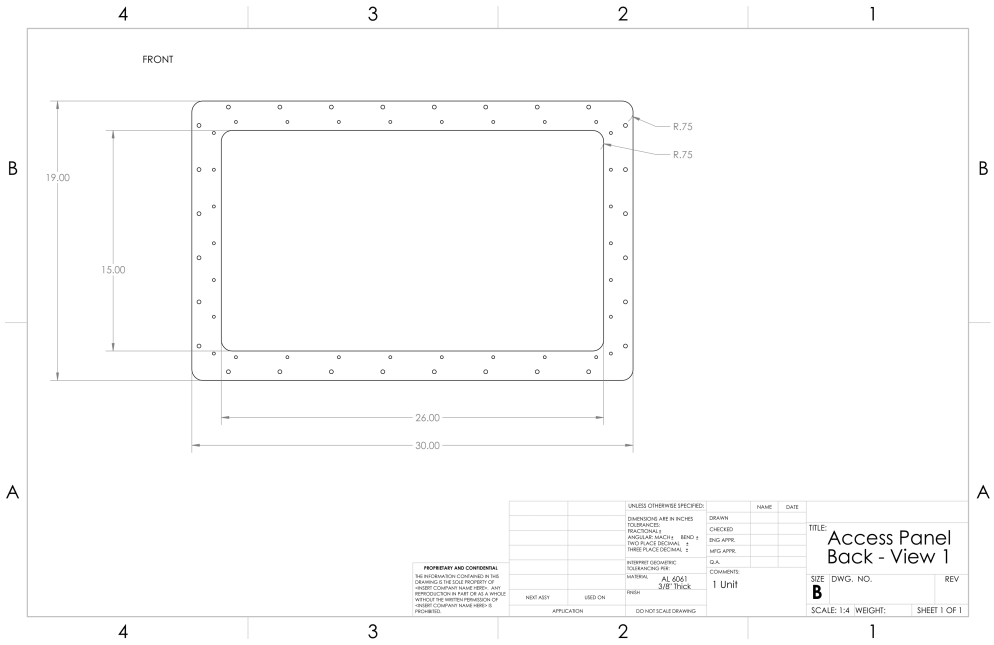

Figure B.3: Access Panel Back - View 1

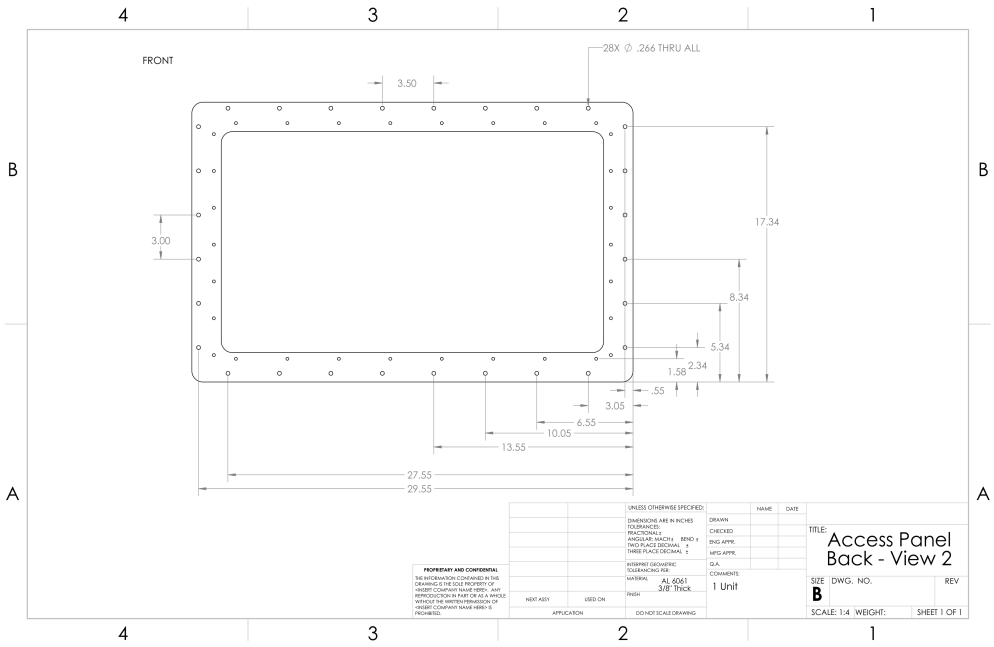

Figure B.4: Access Panel Back - View 2

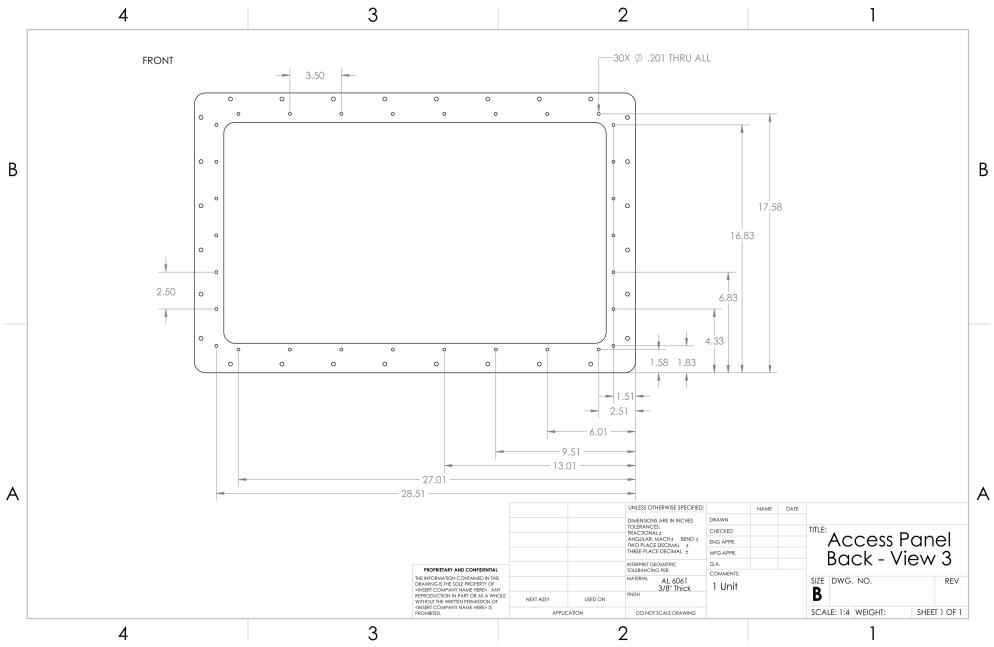

Figure B.5: Access Panel Back - View 3

Frame

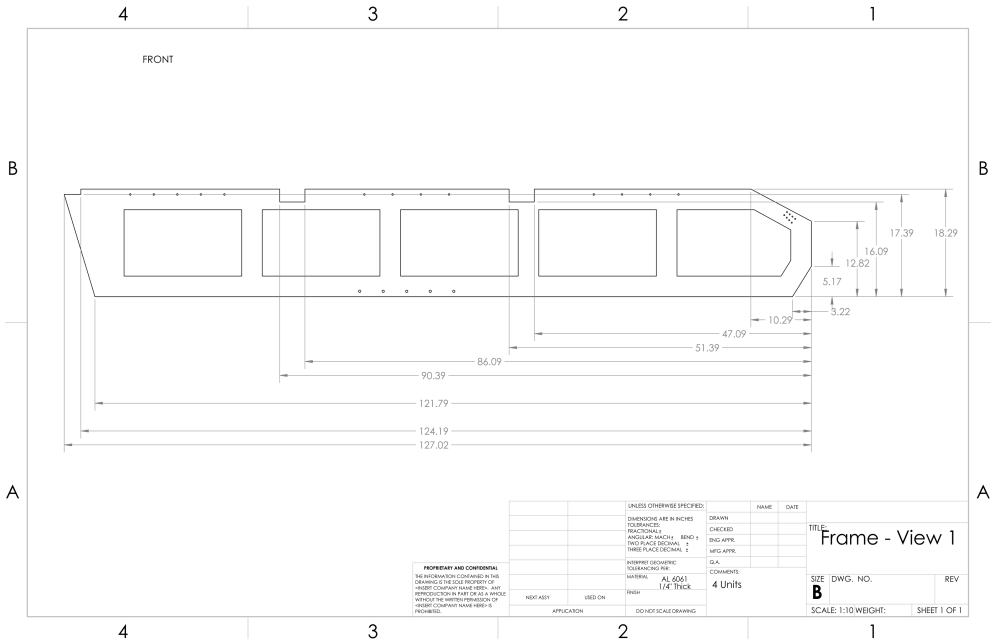

Figure B.6: Frame - View 1

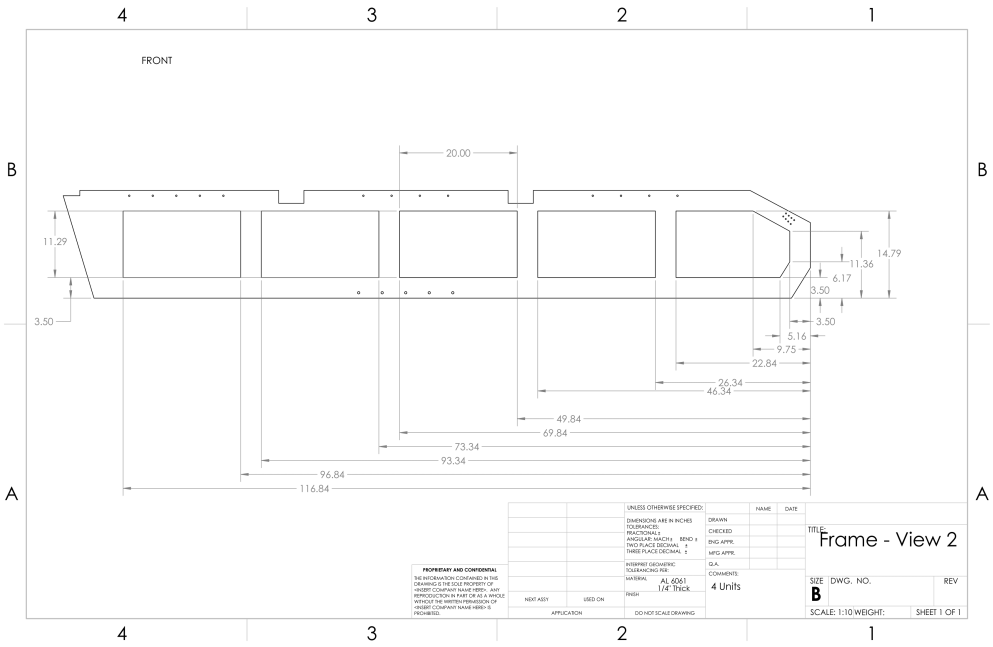

Figure B.7: Frame - View 2

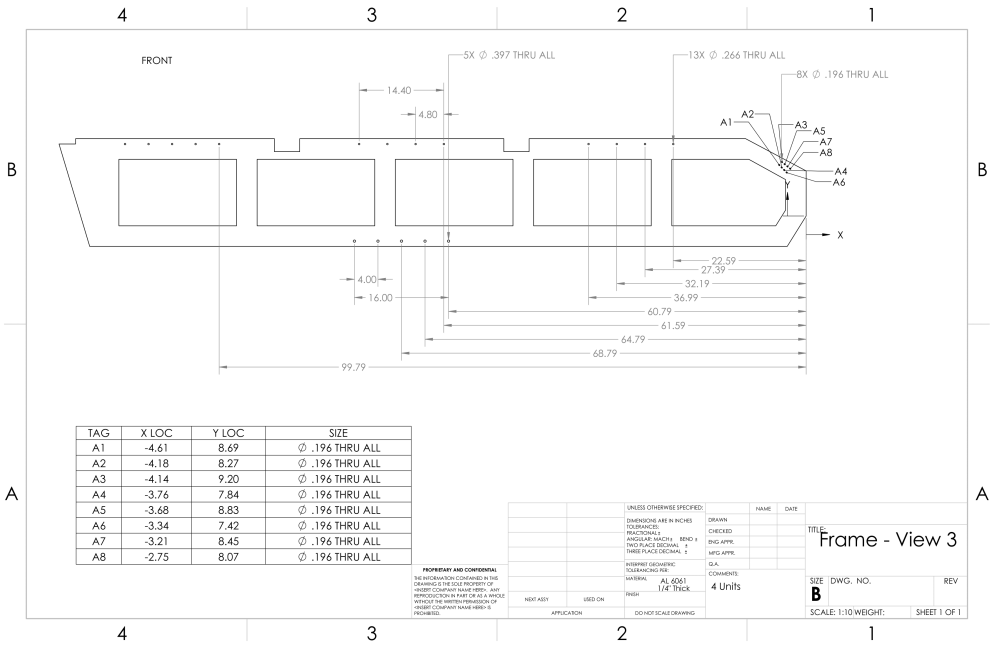

TAG	X LOC	Y LOC	SIZE
A1	-4.61	8.69	∅ .196 THRU ALL
A2	-4.18	8.27	∅ .196 THRU ALL
A3	-4.14	9.20	∅ .196 THRU ALL
A4	-3.76	7.84	∅ .196 THRU ALL
A5	-3.68	8.83	∅ .196 THRU ALL
A6	-3.34	7.42	∅ .196 THRU ALL
A7	-3.21	8.45	∅ .196 THRU ALL
A8	-2.75	8.07	∅ .196 THRU ALL

PROPRIETARY AND CONFIDENTIAL
THE INFORMATION CONTAINED IN THIS DRAWING IS THE SOLE PROPERTY OF <INSERT COMPANY NAME HERE>. ANY REPRODUCTION IN PART OR AS A WHOLE WITHOUT THE WRITTEN PERMISSION OF <INSERT COMPANY NAME HERE> IS PROHIBITED.

UNLESS OTHERWISE SPECIFIED:
DIMENSIONS ARE IN INCHES
TOLERANCES:
FRACTIONAL ±
ANGULAR: MACH ± BEND ±
TWO PLACE DECIMAL ±
THREE PLACE DECIMAL ±
INTERPRET GEOMETRIC TOLERANCING PER:
MATERIAL: AL 6061 1/4" Thick
FINISH
NEXT ASSY | USED ON
APPLICATION | DO NOT SCALE DRAWING

NAME | DATE
DRAWN
CHECKED
ENG APPR.
MFG APPR.
Q.A.
COMMENTS:
4 Units

TITLE: Frame - View 3
SIZE B | DWG. NO. | REV
SCALE: 1:10 WEIGHT: | SHEET 1 OF 1

Figure B.8: Frame - View 3

Plate: Leading Edge (LE)

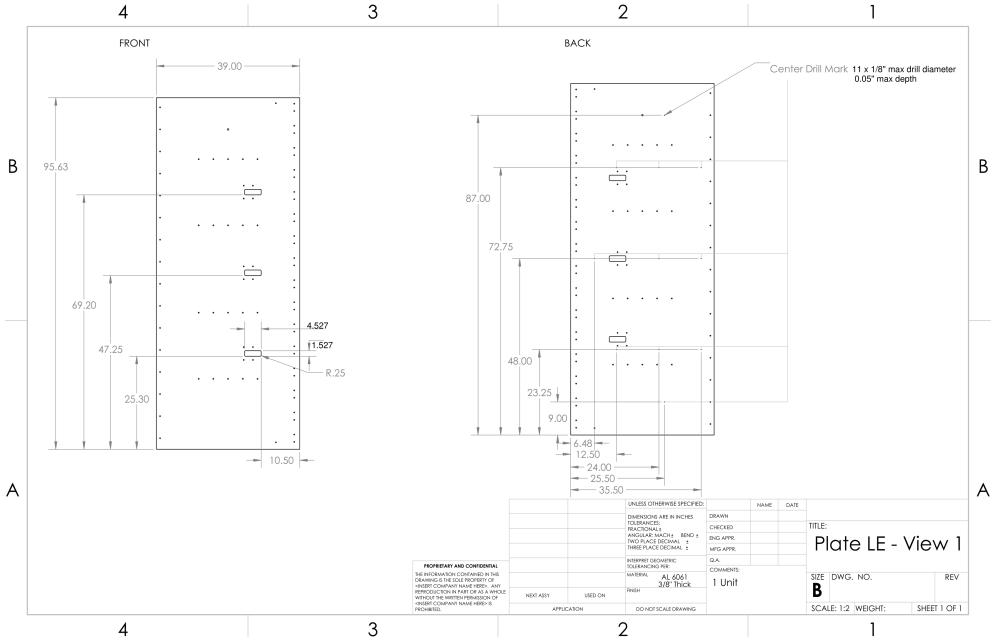

Figure B.9: Plate Leading Edge - View 1

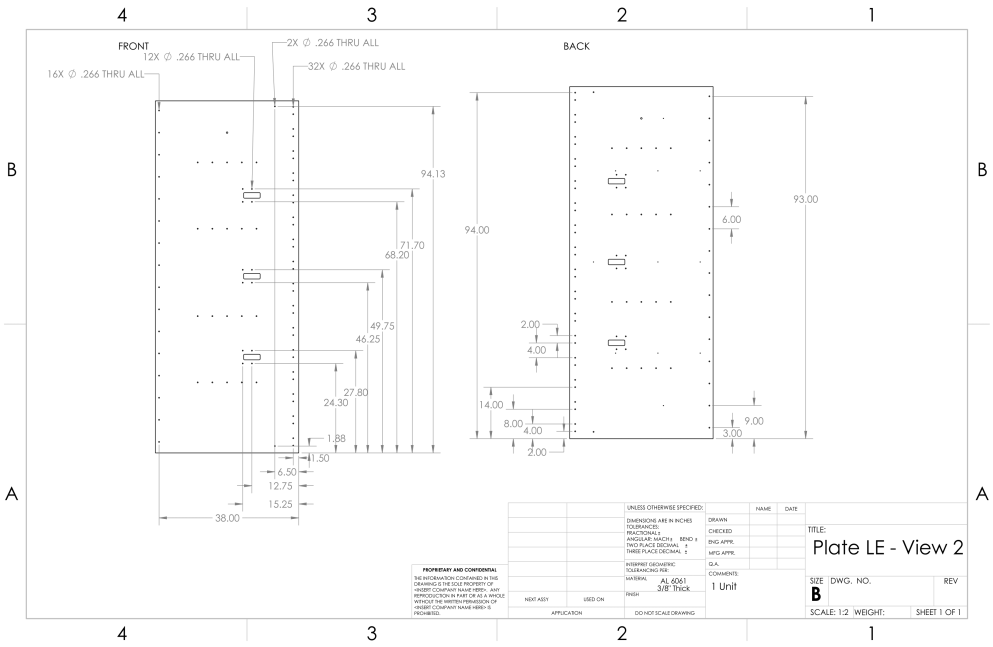

Figure B.10: Plate Leading Edge - View 2

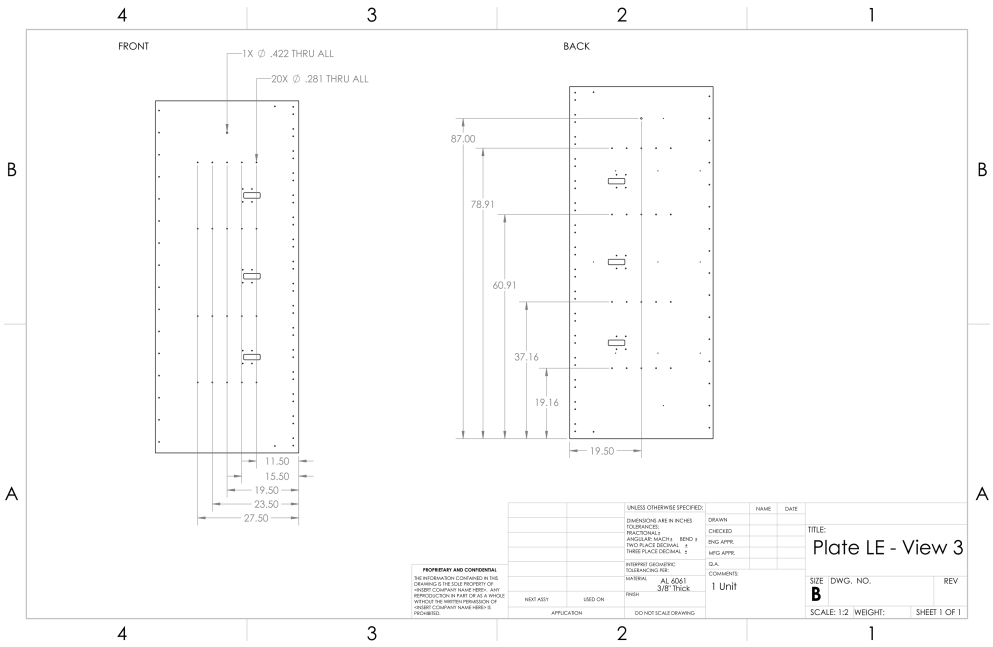

Figure B.11: Plate Leading Edge - View 3

Plate: Middle Section

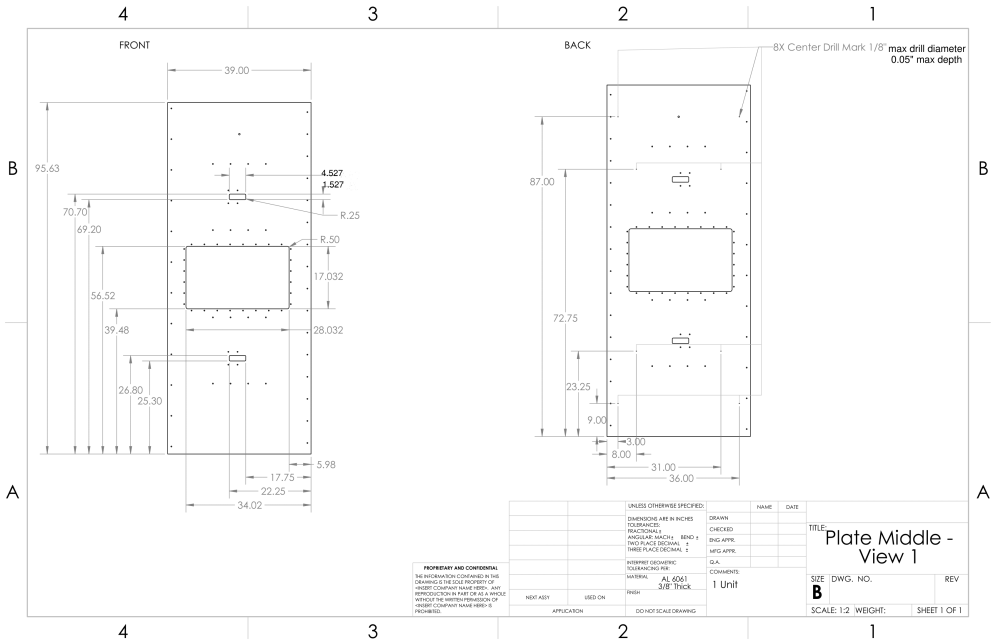

Figure B.12: Plate Middle - View 1

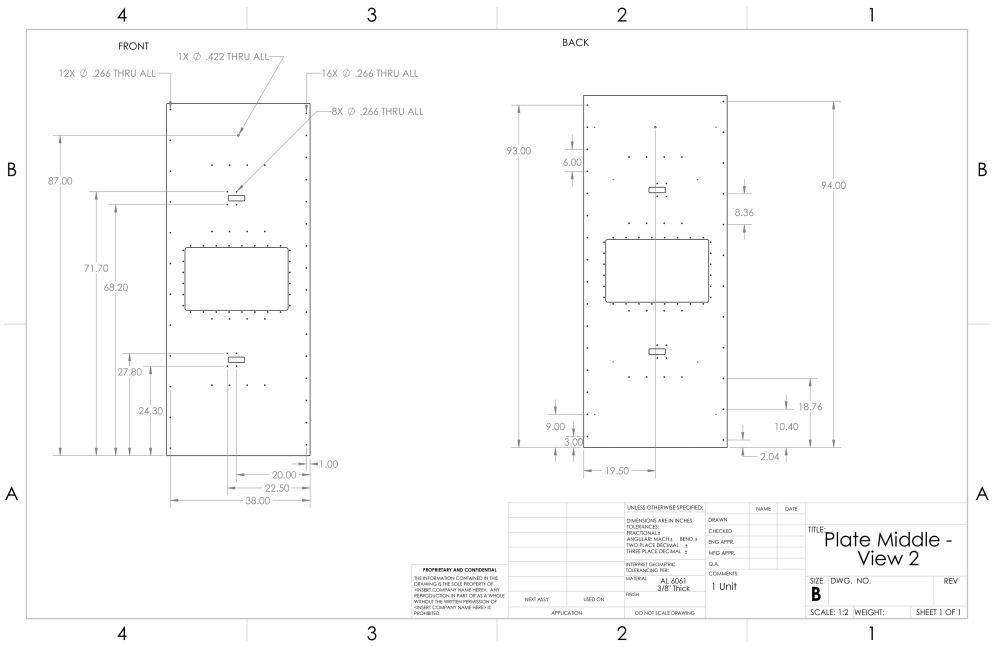

Figure B.13: Plate Middle - View 2

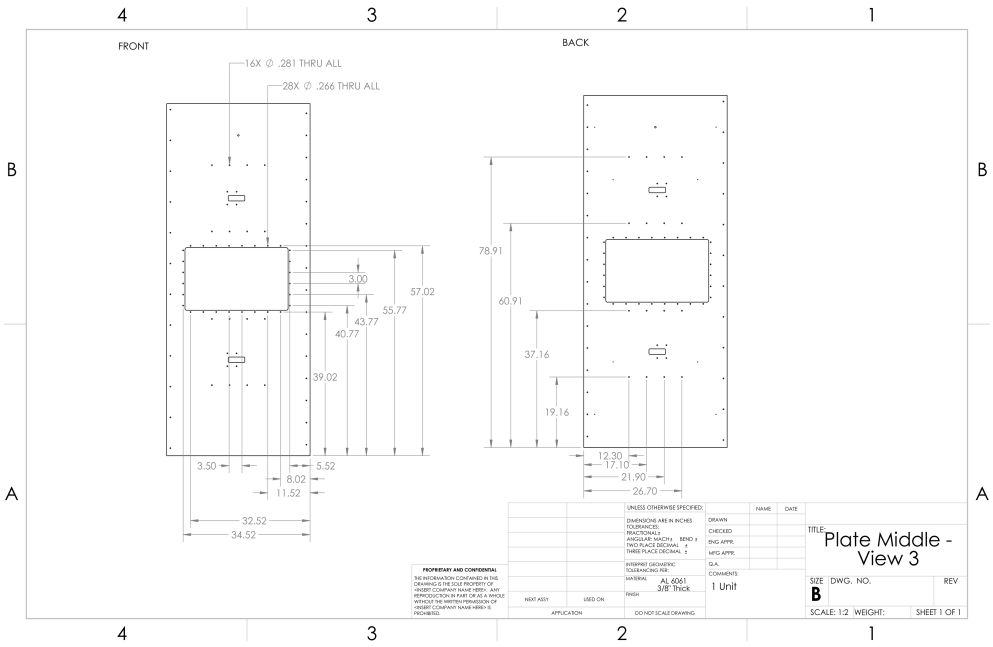

Figure B.14: Plate Middle - View 3

Plate: Trailing Edge (TE)

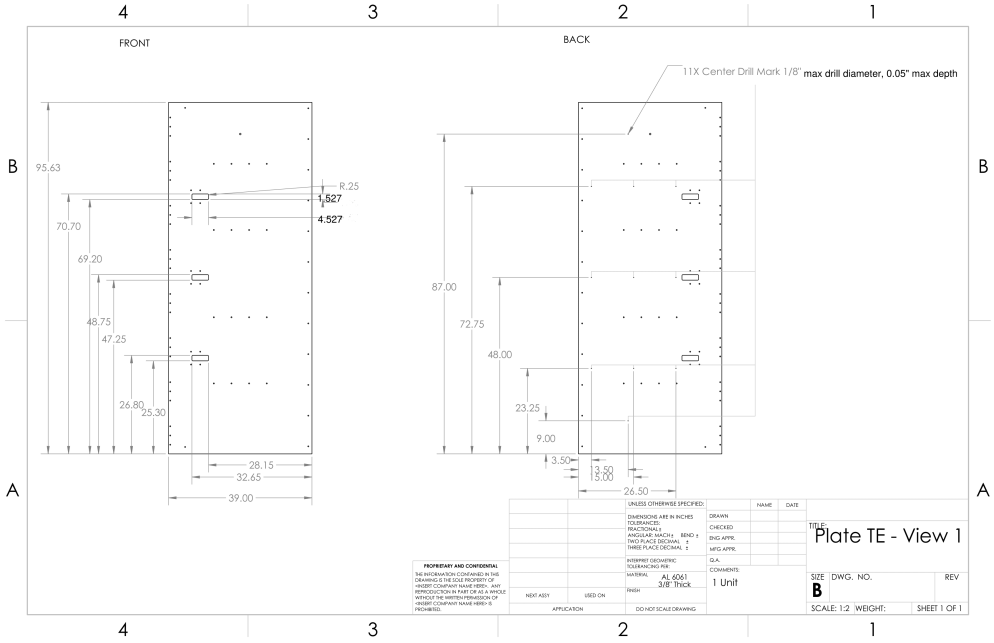

Figure B.15: Plate Trailing Edge - View 1

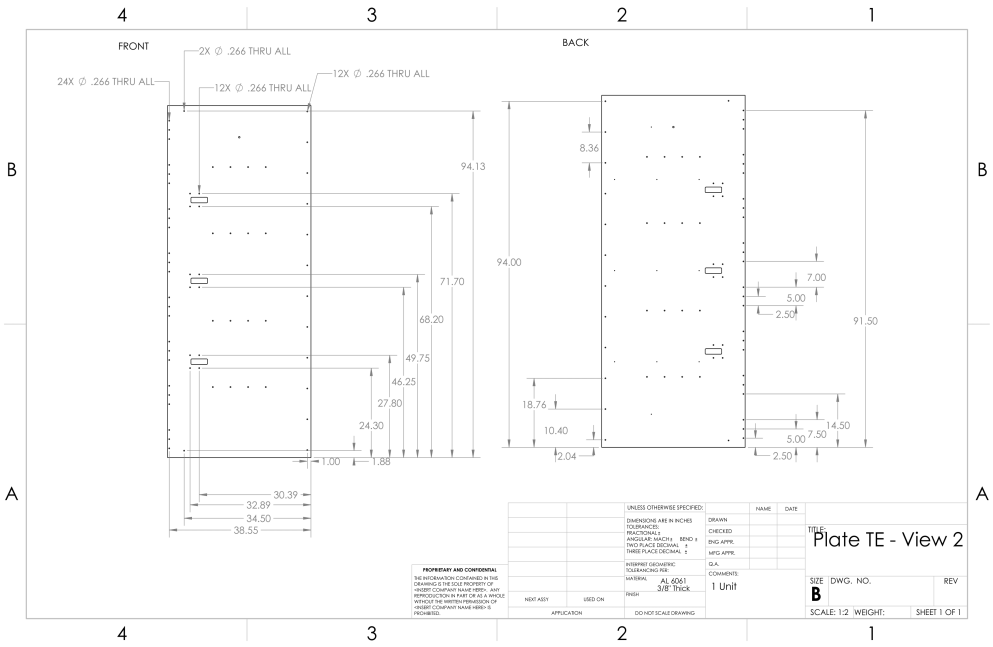

Figure B.16: Plate Trailing Edge - View 2

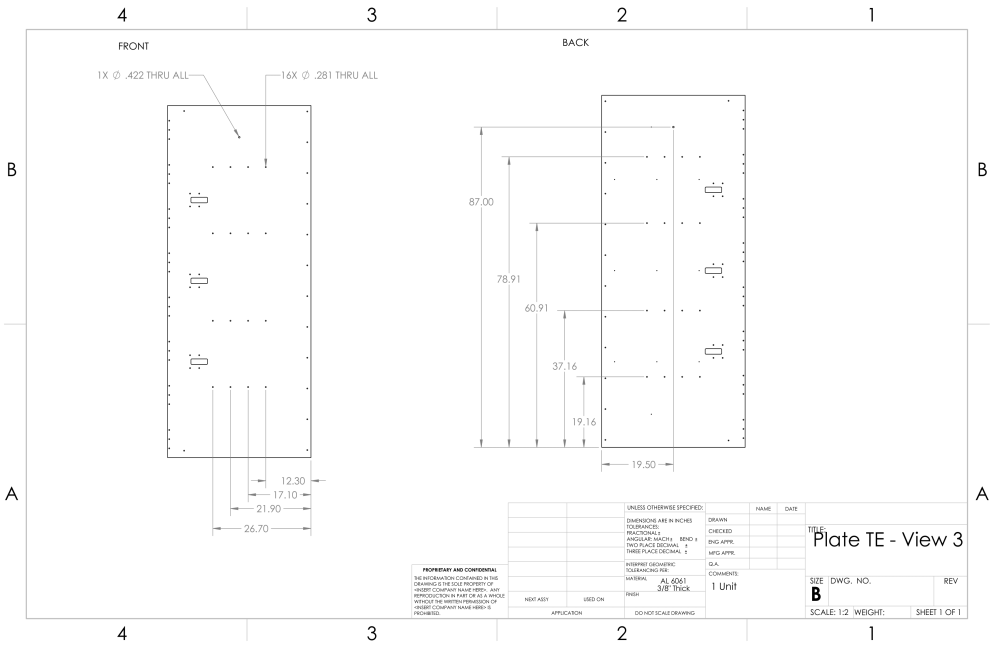

Figure B.17: Plate Trailing Edge - View 3

Wheel Assembly

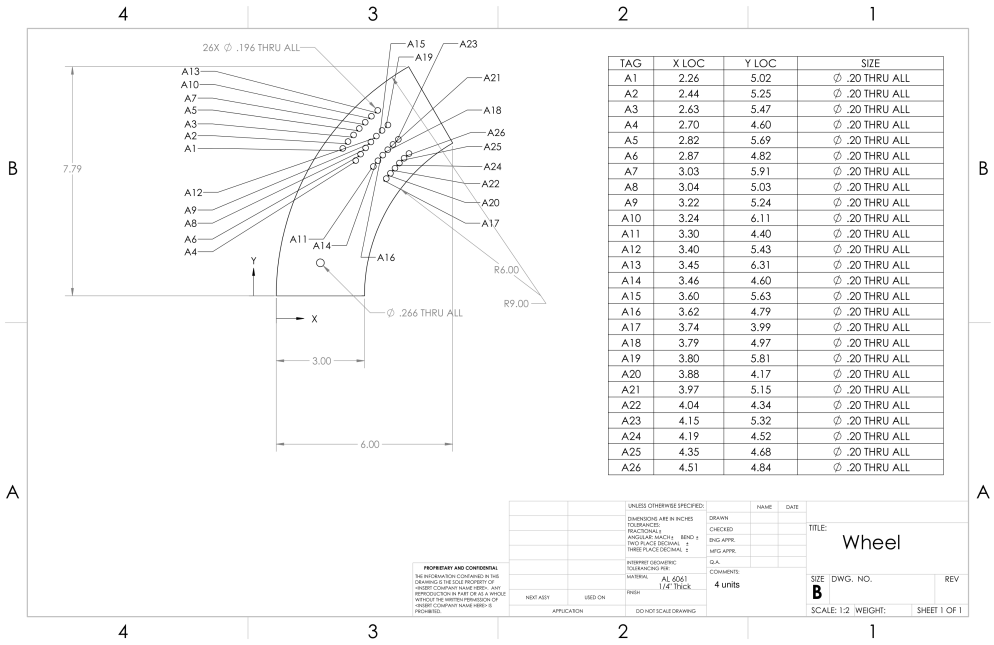

TAG	X LOC	Y LOC	SIZE
A1	2.26	5.02	∅ .20 THRU ALL
A2	2.44	5.25	∅ .20 THRU ALL
A3	2.63	5.47	∅ .20 THRU ALL
A4	2.70	4.60	∅ .20 THRU ALL
A5	2.82	5.69	∅ .20 THRU ALL
A6	2.87	4.82	∅ .20 THRU ALL
A7	3.03	5.91	∅ .20 THRU ALL
A8	3.04	5.03	∅ .20 THRU ALL
A9	3.22	5.24	∅ .20 THRU ALL
A10	3.24	6.11	∅ .20 THRU ALL
A11	3.30	4.40	∅ .20 THRU ALL
A12	3.40	5.43	∅ .20 THRU ALL
A13	3.45	6.31	∅ .20 THRU ALL
A14	3.46	4.60	∅ .20 THRU ALL
A15	3.60	5.63	∅ .20 THRU ALL
A16	3.62	4.79	∅ .20 THRU ALL
A17	3.74	3.99	∅ .20 THRU ALL
A18	3.79	4.97	∅ .20 THRU ALL
A19	3.80	5.81	∅ .20 THRU ALL
A20	3.88	4.17	∅ .20 THRU ALL
A21	3.97	5.15	∅ .20 THRU ALL
A22	4.04	4.34	∅ .20 THRU ALL
A23	4.15	5.32	∅ .20 THRU ALL
A24	4.19	4.52	∅ .20 THRU ALL
A25	4.35	4.68	∅ .20 THRU ALL
A26	4.51	4.84	∅ .20 THRU ALL

Figure B.18: Support Wheel Assembly